Geochemistry Geophysics Geosystems G3
AN ELECTRONIC JOURNAL OF THE EARTH SCIENCES
Published by AGU and the Geochemical Society

Article
Volume 10, Number 10
17 October 2009
Q10009, doi:10.1029/2009GC002570
ISSN: 1525-2027

Common depth of slab-mantle decoupling: Reconciling diversity and uniformity of subduction zones

Ikuko Wada
School of Earth and Ocean Sciences, University of Victoria, P.O. Box 3055, STN CSC, Victoria, British Columbia V8P 5C2, Canada (ikukow@uvic.ca)

Kelin Wang
Pacific Geoscience Centre, Geological Survey of Canada, P.O. Box 6000, Sidney, British Columbia V8L 4B2, Canada

School of Earth and Ocean Sciences, University of Victoria, P.O. Box 3055, STN CSC, Victoria, British Columbia V8P 5C2, Canada

[1] Processes in subduction zones such as slab and mantle-wedge metamorphism, intraslab earthquakes, and arc volcanism vary systematically with the age-dependent thermal state of the subducting slab. In contrast, the configuration of subduction zones is rather uniform in that the arc is typically situated where the slab is ~100 km deep. Toward reconciling the diversity and uniformity, we developed numerical thermal models with a nonlinear mantle rheology for seventeen subduction zones, spanning a large range of slab age, descent rate, and geometry. Where there are adequate observations, such as in Cascadia, northeast Japan, and Kamchatka, we find that surface heat flows can be explained if the interface between the slab and the mantle wedge is decoupled to a depth of 70–80 km. Models with this common decoupling depth predict that the region of high mantle temperatures and optimal fluid supply from the dehydrating slab, both required for melt generation for arc volcanism, occurs where the slab is ~100 km deep. These models also reproduce the variations of the metamorphic, seismic, and volcanic processes with the thermal state of the slab. The shallow decoupling results in a stagnant fore arc whose thermal regime is controlled mainly by the subducting slab. The deeper coupling leads to a sudden onset of mantle wedge flow that brings heat from greater depths and the back arc, and its thermal effect overshadows that of the slab in the arc region. Our results serve to recast the research of subduction zone geodynamics into a quest for understanding what controls the common depth of decoupling.

Components: 20,361 words, 24 figures, 5 tables.

Keywords: subduction zones; thermal models; mantle wedge flow; slab dehydration; intraslab seismicity; volcanic arc.

Index Terms: 8170 Tectonophysics: Subduction zone processes (1031, 3060, 3613, 8413); 8185 Tectonophysics: Volcanic arcs; 8162 Tectonophysics: Rheology: mantle (8033).

Received 20 April 2009; **Revised** 14 July 2009; **Accepted** 4 August 2009; **Published** 17 October 2009.

Wada, I., and K. Wang (2009), Common depth of slab-mantle decoupling: Reconciling diversity and uniformity of subduction zones, *Geochem. Geophys. Geosyst.*, *10*, Q10009, doi:10.1029/2009GC002570.

1. Introduction

[2] Subduction zones show a strong diversity in their geophysical and geological processes (Figure 1). For example, in some subduction zones such as NE Japan, earthquakes within the subducting slab extend to large depths and arc volcanism is highly active, but in other subduction zones such as Cascadia, intraslab earthquakes extend to much shallower depths and arc volcanism is feeble. In contrast to these large variations, the configuration of subduction zones is surprisingly uniform in that the arc is typically located along a relatively narrow zone where the depth of the dipping slab is around 100 km [*Tatsumi and Eggins*, 1995; *England et al.*, 2004]. How to reconcile the diversity and uniformity is still an outstanding issue in the study of subduction zone geodynamics.

[3] Great progress has been made in understanding the diversity of subduction zones. Major differences between subduction zones can be explained by differences in thermally controlled petrologic processes in the subducting slab [e.g., *Kirby et al.*, 1996; *Peacock and Wang*, 1999; *Hacker et al.*, 2003]. Slabs of different ages and hence thermal states go through different pressure-temperature paths during subduction. In general, a younger and warmer slab experiences dehydration reactions at shallower depths. It is now widely accepted that it is mainly the different dehydration depths and different abundance of fluids from the dehydrating slab that give rise to the differences in such processes as intraslab earthquakes and arc volcanism.

[4] Less progress has been made in understanding the uniformity of subduction zone configuration. The relatively uniform subarc slab depth among different subduction zones led to a hypothesis that melt generation is triggered by fluid released from the pressure-dependent dehydration reaction of amphibole in the subducting slab or mantle wedge at ~110 km depth [*Tatsumi*, 1986]. However, with this hypothesis it is difficult to explain why dehydration of other more abundant hydrous minerals in the subducting slab and mantle wedge would not trigger hydration melting at depths other than ~110 km. More recent studies of subarc slab depths by *England et al.* [2004] and *Syracuse and Abers* [2006] paid more attention to explaining what causes the depths in individual subduction zones to deviate from their average depth of about 100 km. However, the important first-order question of why the depths are so similar between subduction zones that are often vastly different in other aspects is yet to be addressed.

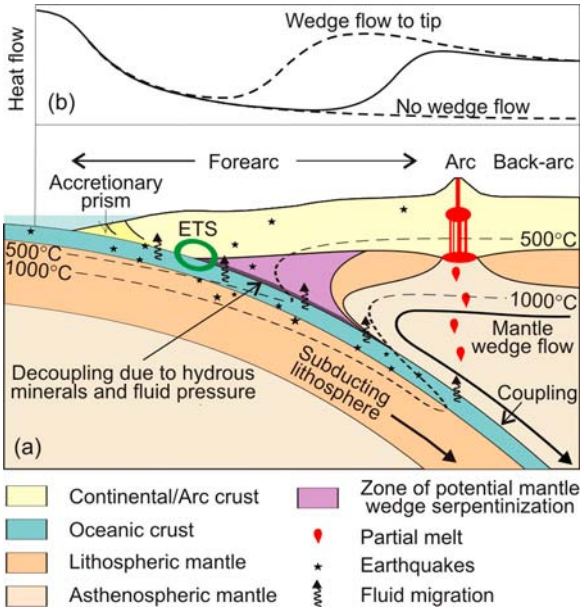

Figure 1. (a) Schematic illustration of a typical warm-slab subduction zone at a continental margin, showing the crustal and upper mantle components and processes that take place in them, and (b) its surface heat flow (solid curve). Green circle in Figure 1a indicates the location of episodic slip and tremor (ETS) observed at Cascadia and Nankai. Models that do not include mantle wedge flow or allow the flow to occur near the tip of the wedge would incorrectly predict the heat flow pattern indicated by dashed curves in Figure 1b. Heat flow patterns for cold-slab subduction zones are similar, except that values near the trench and farther seaward are much lower.

[5] In this study, we try to develop subduction zone thermal models that can reconcile the observed diversity and uniformity. The main challenge we face, as did all previous researchers attempting to tackle this problem, is as follows. To explain the diversity of subduction zones, some key aspects of the thermal structure that we try to reproduce must be strongly dependent on the thermal state of the subducting slab; yet, to explain the uniformity, some other key aspects must be independent of the slab's thermal state. We will demonstrate that a thermal model featuring a sharp contrast between a cold fore arc and a hot volcanic arc, which is consistent with heat flow observations (Figure 1), has these seemingly self-contradicting characteristics. The key parameter that controls this sharp contrast is the maximum depth of decoupling (MDD) between the subducting slab and the overriding mantle wedge. In most of the fore arc where the slab and the mantle wedge are decoupled, the thermal regime is strongly controlled by the thermal state of the slab. Beneath

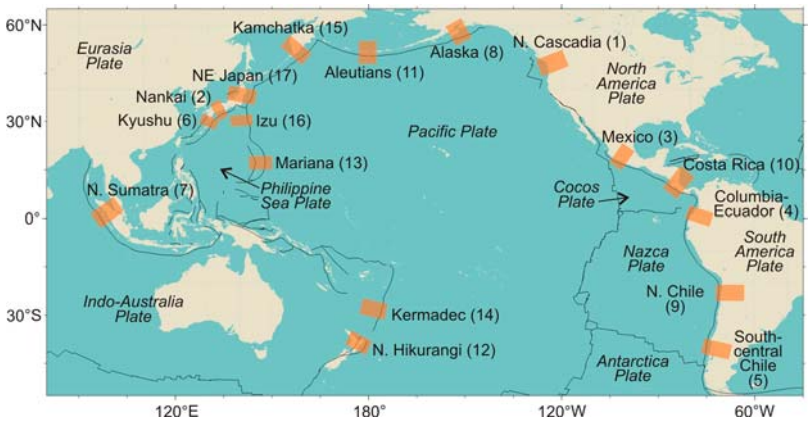

Figure 2. Map showing the locations of seventeen subduction zone corridors (orange areas) investigated in the present study. The number in parentheses indicates the index number of the subduction zone.

the arc where the slab and mantle wedge are coupled, the thermal regime is controlled mainly by solid-state viscous flow of the mantle wedge and is nearly independent of the thermal state of the slab. We will show that a common MDD of 70–80 km can reconcile the observed diversity and uniformity of subduction zones.

[6] In the following, we will first provide a synthesis of geophysical and geological observations from a number of subduction zones. These observations illustrate the diversity of the above mentioned processes and the uniformity of subduction zone configuration and help us identify important trends. Seventeen subduction zones are considered, including Alaska, Aleutians, northern Cascadia, south central (SC) and northern Chile, Colombia-Ecuador, northern Costa Rica, northern Hikurangi, Izu, Kamchatka, Kermadec, Kyushu, Mariana, Mexico, Nankai, northeast (NE) Japan, and Sumatra (Figure 2). We will then develop numerical models for these subduction zones and illustrate that a common depth of decoupling is consistent with the observations.

2. Relation Between Subduction Zone Processes and the Slab Thermal Parameter

[7] Most geophysical and geological processes in subduction zones depend strongly on temperature, and the variations in these processes correlate with the thermal state of the subducting slab. Here, we examine the trends of some of these observations as a function of the thermal state of the subducting slab, which is approximately described by the thermal parameter, φ, a product of the age and descent rate of the slab [*McKenzie*, 1969; *Molnar et al.*, 1979; *Kirby et al.*, 1996]. Generally, the higher the φ value, the cooler is the subducting slab at a given depth. On the basis of the availability of geological and geophysical observations and structural and kinematic information, we select seventeen subduction zones for this study. The relatively large number of subduction zones and the wide range of φ values spanned by them are ideal for examining the trends of the observations.

[8] For the calculation of φ for the seventeen subduction zones, we use the age of the subducting slab determined from magnetic isochrons on the oceanic plate as reported in the literature (Table 1), except for northern Hikurangi and Kermadec where the magnetic isochrons on the incoming plate are not identifiable at present. The old age ($\sim$100 Ma) of the adjacent oceanic crust and tectonic reconstruction suggest that the subducting plates at these two margins are no younger than 100 Ma [*Davy and Wood*, 1994; *Müller et al.*, 1997]. The thermal states of old oceanic plates ($>\sim$80 Ma) are uniformly cold (surface heat flow of $<$60 mW/m^2), and their differences are negligibly small. Thus, we assume a slab age of 100 Ma for these two margins.

[9] The descent rate of the slab is the product of the margin-normal convergence rate and the sine of the dip of the slab. We calculate the convergence rates by using the global plate motion model NUVEL-1A [*DeMets et al.*, 1990, 1994] for the seventeen subduction zones except for Nankai, Kyushu, Mexico, Costa Rica and Sumatra. We use a relative plate motion model determined by *Zang et al.* [2002] for Nankai and Kyushu and one by *DeMets* [2001] for Mexico and Costa Rica. These two models are constrained by newly obtained plate motion data in addition to those

Table 1. Summary of Subduction Zone Parameters

Index	Subduction Zone	φ/100 (km)	Slab Age at Trench (Ma)	References for Slab Age	Convergence Rate (mm/yr)	Subduction Direction[a] (°)	Subduction Rate[b] (mm/yr)	Slab Dip[c] (°)	Subarc Slab Depth (km)	References for Subarc Slab Depth
1	N. Cascadia	2.2	8	*Wilson* [1988]	43	62	43	40	90	*McCrory et al.* [2004]
2	Nankai	3.9	15	*Okino et al.* [1994]	46	315	44	36	90	See the text.[d]
3	Mexico	4.2	13	*Kostoglodov and Bandy* [1995]	55	35	55	36	110	*Currie et al.* [2002]
4	Colombia-Ecuador	4.5	16	*Hardy* [1991]	65	80	46	38	110	See the text.[d]
5	SC Chile	8.6	25	*Tebbens et al.* [1997]	80	79	71	29	80	*Syracuse and Abers* [2006]
6	Kyushu	10.5	27	*Okino et al.* [1994]	50	315	47	56	105 ± 5	*England et al.* [2004]
7	N. Sumatra	11.2	50	*Cande and Kent* [1995]	55	12	40	34	115 ± 5	*England et al.* [2004]
8	Alaska	13.3	46	*Atwater* [1989]	55	341	47	38	85 ± 5	*England et al.* [2004]
9	N. Chile	13.4	48	*Müller et al.* [1997]	80	78	78	21	115 ± 5	*England et al.* [2004]
10	N. Costa Rica	17.1	24	*Barckhausen et al.* [2001]	85	23	80	63	95	*Syracuse and Abers* [2006], *Peacock et al.* [2005]
11	Aleutians	22.8	55	*Müller et al.* [1997]	72	319	54	50	80 ± 5 - 105 ± 6[e]	*England et al.* [2004]
12	N. Hikurangi	22.9	100	See the text.	41	266	29	52	85	*Reyners et al.* [2006, 2007]
13	Mariana	36.7	140	*Müller et al.* [1997]	39	310	30	61	115 ± 10	*England et al.* [2004]
14	Kermadec	47.3	100	See the text.	60	272	57	56	95 ± 5	*England et al.* [2004]
15	Kamchatka	47.8	100	*Müller et al.* [1997]	77	308	76	39	95 ± 5	*England et al.* [2004]
16	Izu	52.2	140	*Müller et al.* [1997]	55	286	51	47	130 ± 6	*England et al.* [2004]
17	NE Japan	52.3	130	*Müller et al.* [1997]	83	297	83	29	100 ± 5	*England et al.* [2004]

[a] Subduction direction is measured from north.
[b] The margin-normal component of the convergence rate is used.
[c] The average dip between 75 and 140 km depths is used.
[d] The authors extrapolated the subarc slab depth from the existing slab geometry model for the shallow part of the slab and from limited intraslab earthquakes in the EHB catalog.
[e] *England et al.* [2004] determined the subarc slab depth for the western, central, and eastern segments of the Aleutian margin. The depth range shown is from the shallowest (eastern segment) to the deepest (western segment) of the three. A subarc slab depth of 95 km is used in the thermal model for Aleutians.

used to constrain NUVEL-1A and are more accurate than NUVEL-1A for the relatively plate motions at these four margins. In Sumatra, the Australia plate subducts beneath the Sunda tectonic block, which is not differentiated from the adjacent Eurasia plate in NUVEL-1A, and therefore we instead use the relative plate motions constrained by GPS data for this margin by *Bock et al.* [2003]. For the calculation of φ, we use the average dip between 75 and 140 km depths; for our purpose, the absolute depths are unimportant as long as the choice is made consistently between different subduction zones.

2.1. Low-Velocity Layer Representing the Untransformed Subducting Crust

[10] The basalt-eclogite transformation in the subducting crust signals the peak of slab dehydration reactions and results in an increase in density and seismic velocities. Where resolution allows, seismological studies have revealed the presence of a narrow dipping layer of relatively low seismic-wave speed along the top of the subducting slab that is commonly interpreted to be the basaltic oceanic crust that has not transformed to eclogite [*Fukao et al.*, 1983] (Figure 3a). In Cascadia, analyses of receiver functions [*Cassidy and Ellis*, 1993] and scattered teleseismic body waves [*Bostock et al.*, 2002] indicate the presence of a low-velocity layer (LVL) down to 45–75 km depths. In Nankai, later P and S wave phases that traveled through the untransformed subducting crust indicate that an LVL extends to ~60 km depth [*Hori et al.*, 1985; *Hori*, 1990; *Ohkura*, 2000]. In northern Chile, receiver function analyses show that an LVL extends to ~120 km depth [*Yuan et al.*, 2000; *Bock et al.*, 2000]. In Alaska, analyses of scattered teleseismic body waves [*Rondenay et al.*, 2008] and receiver functions [*Abers et al.*, 2006] indicate that an LVL extends to ~120 km depth. In NE Japan, analyses of PS-P time data [*Matsuzawa et al.*, 1986] and receiver functions [*Kawakatsu and Watada*, 2007] show that an LVL extends to 100–150 km depths. The downdip extent of this layer is clearly deeper in the colder and older slabs in northern Chile, Alaska, and NE Japan than in younger and warmer slabs in Cascadia and Nankai (Figure 3a). This trend agrees with petrologic predictions based on thermal models [e.g., *Peacock and Wang*, 1999; *Hacker et al.*, 2003].

[11] *Abers* [2005] used body wave dispersion to determine the velocity contrast of an LVL with its surroundings for three depth ranges (0–100, 100–150, and >200 km) in Nicaragua (near our study region of northern Costa Rica), Aleutians, Alaska, Mariana, Kamchatka, and NE Japan. The results can be interpreted to indicate the presence of an LVL to at least 150 km depth at the six margins although the exact maximum depth is undetermined because of the large depth bins used in the study. The slabs in all the six subduction zones are relatively cold, and the inferred, relatively deep downdip extent of the LVL is consistent with those reported for other cold slab subduction zones (Figure 3a). Furthermore, in Nicaragua and Alaska where the slabs are warmest among the six subduction zones, the velocity contrast of the thin layer with its surroundings practically disappears for the >150 km depth bin, indicating that the downdip limit of the layer is within the 100–150 km range, also consistent with the general trend illustrated in Figure 3a.

2.2. Mantle Wedge Serpentinization

[12] In the fore-arc mantle wedge, hydrous minerals such as serpentine (antigorite, chrysotile, and lizardite), chlorite, talc, brucite, magnetite and amphibole can form, provided that the mantle wedge is cold and there is sufficient fluid supply from the dehydrating slab [*Hacker et al.*, 2003]. Antigorite is stable between ~300°C and ~700°C [*Ulmer and Trommsdorff*, 1995] and is expected to be the most abundant hydrous mineral in a hydrated fore-arc mantle wedge at continental convergent margins [*Hyndman and Peacock*, 2003]. The other two serpentine species chrysotile and lizardite may also form in the mantle wedge but are stable only at temperatures lower than ~300°C [*Evans*, 1977, 2004].

[13] Serpentinization of the mantle wedge results in a decrease in density and seismic velocities. The decrease in the velocity is more prominent for the S wave, resulting in a higher ratio of P to S wave velocities (Vp/Vs) and hence a higher Poisson's ratio [*Christensen*, 2004, and references therein]. Serpentinization also results in increased magnetic susceptibility of the mantle due to the formation of magnetite as a by-product of serpentinization [*Hyndman and Peacock*, 2003, and references therein].

[14] Low Vp and Vs values observed in the Cascadia fore-arc mantle are interpreted as to indicate serpentinization (20–60%) [*Bostock et al.*, 2002; *Brocher et al.*, 2003; *Ramachandran et al.*, 2005]. This interpretation is supported by high-amplitude, long-wavelength positive magnetic anomalies and

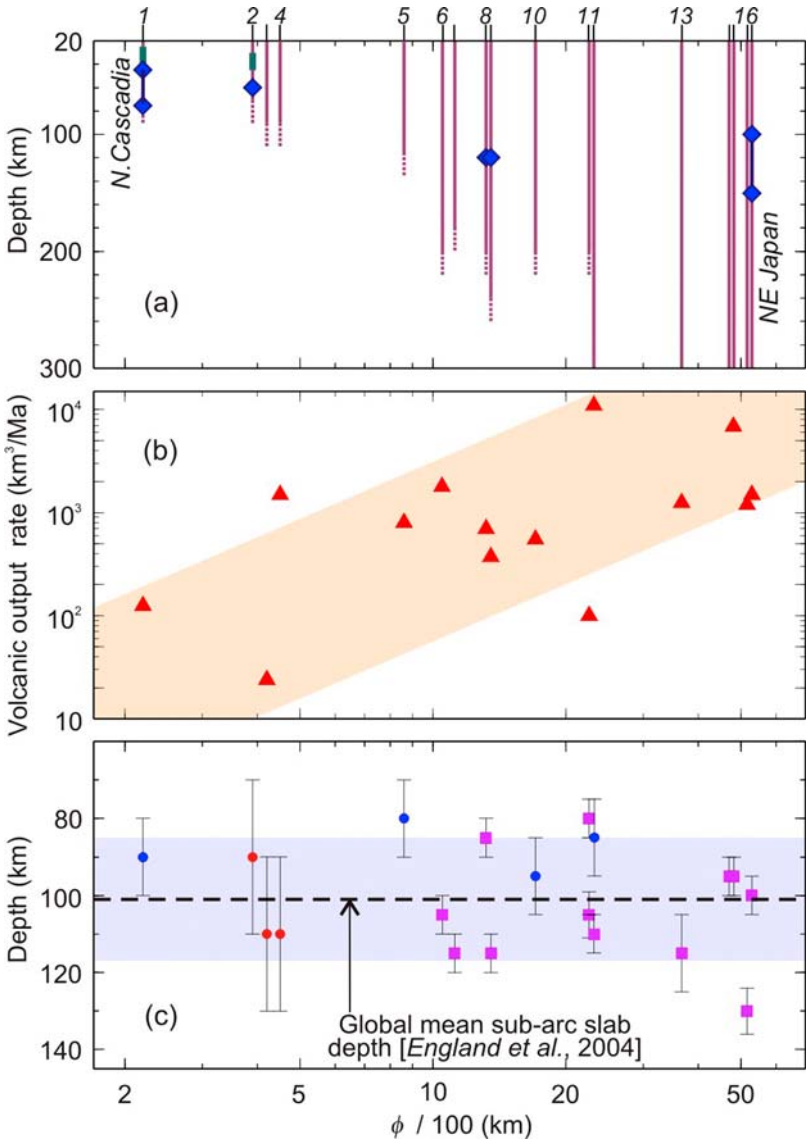

Figure 3. Variations of the observed characteristic parameters of geophysical processes in subduction zones with the thermal parameter of the subducting slab, φ. Index numbers (Figure 2), which are shown for some subduction zones at the top, are given to subduction zones in the order of increasing φ (Table 1): 1, northern Cascadia; 2, Nankai; 3, Mexico; 4, Columbia-Ecuador; 5, SC Chile; 6, Kyushu; 7, northern Sumatra; 8, Alaska; 9, northern Chile; 10, northern Costa Rica; 11, Aleutians; 12, northern Hikurangi; 13, Mariana; 14, Kermadec; 15, Kamchatka; 16, Izu; 17, NE Japan. (a) Observed maximum depth of a low-velocity layer in the subducting crust (blue diamond) and depth range of intraslab seismicity (purple lines). Dashed purple lines indicate uncertainties in the maximum depth. Green lines indicate the depth range of ETS events in northern Cascadia [*Kao et al.*, 2005] and Nankai [*Shelly et al.*, 2006]. (b) Long-term volcanic output rates of volcanic arc [*Crisp*, 1984; *White et al.*, 2006]. (c) Subarc slab depths determined by *England et al.* [2004] (purple squares) and others (blue circles) and those extrapolated by the authors (red circles) with error bars (see Table 1). The dashed horizontal line and light blue area indicate the global mean depth of 101 km and a standard deviation of 16 km, respectively, from *England et al.* [2004]. All the parameter values and their references except for the depth range of ETS in Cascadia and Nankai are listed in Table 2.

negative gravity anomalies in the Cascadia fore arc [*Blakely et al.*, 2005]. Serpentinization of the fore-arc mantle wedge has also been inferred from seismic observations in Nankai (50–70%) [*Kamiya and Kobayashi*, 2000; *Seno et al.*, 2001], Kyushu (20–30%) [*Xia et al.*, 2008], northern Chile (0–12%) [*Graeber and Asch*, 1999; *Carlson and Miller*, 2003], and Costa Rica (15–25%) [*DeShon and Schwartz*, 2004; *Carlson and Miller*, 2003], from magnetic and gravity anomalies in Alaska

[*Saltus et al.*, 1999], and from the presence of serpentine mud volcanoes in the fore-arc region of the Izu and Mariana margins [*Fryer*, 1996]. The presence of a serpentinized fore-arc mantle wedge is proposed to explain the lack of velocity contrast between the continental crust and the underlying mantle in SC Chile [*Groß et al.*, 2008]. In contrast, a relatively dry mantle wedge corner and thus a minor degree of serpentinization are reported for northern Hikurangi [*Eberhart-Phillips et al.*, 2008] and in most parts of NE Japan [e.g., *Miura et al.*, 2005]. There has been no investigation on mantle wedge serpentinization for our study regions of the other six subduction zones. Although further observations are required for the global distribution of mantle wedge serpentinization, it appears at present that evidence for serpentinization is more readily observed in subduction zones with warm slabs, possibly indicating a greater fluid supply beneath the fore-arc mantle wedge.

2.3. Intraslab Earthquakes and Nonvolcanic Seismic Tremor

[15] The depth range of intraslab earthquakes varies greatly among subduction zones. For most of the seventeen subduction zones, we infer the maximum depth of intraslab seismicity from the global earthquake catalog of *Engdahl et al.* [1998] (hereinafter referred to as the EHB catalog), in which earthquake hypocenters are located using teleseismic networks. In northern Cascadia, Nankai, Kyushu, SC Chile, and Costa Rica, the number of intraslab earthquakes in the EHB catalog is small mostly because of the paucity of events that are large enough to be located by teleseismic networks. For these subduction zones, we infer the depth range from intraslab earthquake hypocenter locations determined by local networks (see Table 2 for references). The maximum depth may be slightly underestimated because earthquake catalogs that are used to determine this depth exclude events that do not meet all the criteria for hypocenter determination. We express uncertainties in the maximum depth by dashed lines in Figure 3a. The maximum depth of intraslab seismicity generally increases with φ from 70 km to greater than 300 km.

[16] Stresses cause failure of geologic material, but they alone do not determine whether the failure occurs seismically or aseismically. Laboratory experiments indicate that the high confining pressure at the depths of intermediate-depth (about 50–300 km depths) intraslab earthquakes tends to inhibit seismic rupture of geologic materials. It is thus hypothesized that fluid released during the dehydration of hydrous minerals in the subducting slab elevates pore fluid pressure, reducing the effective pressure and facilitating seismic rupture [e.g., *Kirby et al.*, 1996]. This process is commonly referred to as "dehydration embrittlement," a term originally used to describe a laboratory observation that fluid release causes an immediate change from ductile to brittle deformation. According to this hypothesis, the presence of fluid causes rock failure to occur seismically, controlling the distribution of intraslab earthquakes.

[17] Intraslab earthquakes at relatively shallow depths occur in two subparallel bands (double seismic zone) in many subduction zones [e.g., *Brudzinski et al.*, 2007]. They are thought to represent seismicity in the subducting crust and upper mantle separated by an aseismic core [*Hacker et al.*, 2003]. The separation between the two bands tends to be greater for older and colder slabs, and the lower band is located several tens of kilometers away from the slab surface in very old and cold slabs (e.g., NE Japan) [e.g., *Brudzinski et al.*, 2007]. Dehydration embrittlement of the subducting crust and mantle is proposed to cause earthquakes in the upper and lower bands, respectively, although how the initially anhydrous oceanic mantle becomes hydrated to the depths of several tens of kilometers prior to subduction is not well understood [*Peacock*, 2001; *Yamasaki and Seno*, 2003]. Dehydration reactions are expected to extend to greater depths in higher-φ colder slabs than in lower-φ warmer slabs [*Kirby et al.*, 1996], and thus the increase in the maximum depth of intraslab seismicity with φ (Figure 3a) supports the hypothesis of dehydration embrittlement in both the subducting crust and mantle.

[18] Nonvolcanic seismic tremor and associated silent slip of the subduction interface, together referred to as episodic tremor and slip (ETS) events, occur near the tip of the mantle wedge in the warm-slab Cascadia and Nankai subduction zones (Figure 3a). ETS-like events are also reported to occur in Mexico [*Larson et al.*, 2007; *Payero et al.*, 2008], which is another warm-slab subduction zone. In contrast, ETS events are not observed in cold-slab subduction zones, such as NE Japan and northern Hikurangi. It is suggested that ETS may be related to free fluids released from the dehydrating slab although the exact mechanism is unknown [*Obara*, 2002; *Kao et al.*, 2005; *Shelly et al.*, 2007; *Wada et al.*, 2008]. The occurrence of ETS in warm-slab subduction zones may thus be

Table 2. Geological and Geophysical Observations

Index	Subduction Zone	References for Heat Flow Data in the Fore-Arc–Arc Region	Maximum Downdip Extent of a Low-Velocity Layer (km)	References for Maximum Downdip Extent	Maximum Depth of Intraslab Seismicity (km)	References for Maximum Depth of Intraslab Seismicity	Volcanic Output Rate (km^3/Ma)	Eruption Duration (Ma)	Measured Volcano
1	N. Cascadia	*Currie et al.* [2004], *Wang et al.* [1995]	45–75	*Bostock et al.* [2002], *Cassidy and Ellis* [1993]	70	*Cassidy and Waldhauser* [2003]	125[a]	1.29	Mt. Baker
2	Nankai	*Tanaka et al.* [2004]	60	*Hori et al.* [1985], *Hori* [1990], *Ohkura* [2000]	70	*Nakamura et al.* [1997], *Baba et al.* [2002]			
3	Mexico	GHFD[b]			90	*Engdahl et al.* [1998]	24[a]	1	Zitacuaro-Valle de Bravo
4	Colombia-Ecuador	*Marcaillou et al.* [2006]			90	*Engdahl et al.* [1998]	1500[a]	0.002	Tungurahua
5	SC Chile	*Grevemeyer et al.* [2003], GHFD			115	*Haberland et al.* [2006], *Engdahl et al.* [1998]	800 ± 180[a]	0.65	Calabozos caldera
6	Kyushu	*Tanaka et al.* [2004]			200	*Zhao et al.* [2000], *Engdahl et al.* [1998]	1800 ± 500[c]	0.014	Sakurajima
7	N. Sumatra	GHFD			180	*Engdahl et al.* [1998]			
8	Alaska	GHFD	120	*Rondenay et al.* [2008], *Abers et al.*, [2008]	200	*Engdahl et al.* [1998]	700[a]	0.89	Regional average
9	N. Chile	GHFD	120	*Yuan et al.* [2000], *Bock et al.* [2000]	240	*Engdahl et al.* [1998]	374[a]	10	per 100 km
10	N. Costa Rica	*Langseth and Silver* [1996], *Kimura et al.* [1997]			200	*Peacock et al.* [2005]	550[c]	4.73e-5	Arenal
11	Aleutians	GHFD			200	*Engdahl et al.* [1998]	100[a]	3.5	per 100 km
12	N. Hikurangi	GHFD, *Townend* [1997]			>300	*Engdahl et al.* [1998]	11000 ± 1000[c]	0.61	Taupo
13	Mariana	GHFD			>300	*Engdahl et al.* [1998]	1250[c]	5	per 100 km
14	Kermadec	*von Herzen et al.* [2001]			>300	*Engdahl et al.* [1998]			
15	Kamchatka	*Tanaka et al.* [2004]			>300	*Engdahl et al.* [1998]	6900[a]	0.01	Tolbachik
16	Izu				>300	*Engdahl et al.* [1998]	1500[a]	0.025	Oshima
17	NE Japan	*Tanaka et al.* [2004]	100–150	*Matsuzawa et al.* [1986], *Kawakatsu and Watada* [2007]	>300	*Engdahl et al.* [1998]	1200 ± 300[c]	0.3	Asama

[a] Values are from *White et al.* [2006].
[b] GHFD is an abbreviation for Global Heat Flow Database [*Pollack et al.*, 1993; Global Heat Flow Database, 2004].
[c] Values are from *Crisp* [1984].

associated with the shallow dehydration of the warm subducting slabs.

2.4. Volcanic Output Rate

[19] The intensity of arc volcanism is highly variable among different subduction zones. On the basis of the hypothesis that arc crust is formed through magmatism, arc magma production rates have been estimated indirectly from the growth rates of arc crust that are inferred primarily from seismic and gravity studies [e.g., *Dimalanta et al.*, 2002; *Hochstein*, 1995; *Taira et al.*, 1998]. These estimates depend on the inferred thickness and width of the crust across the arc. In the present study, instead of using indirect inferences on arc magma production rates, we consider the long-term volumetric volcanic output rate of a volcano or a unit length (100 km) of the volcanic arc in subduction zones compiled by *Crisp* [1984] and more recently by *White et al.* [2006] (Table 2). This rate accounts mainly for the extrusive portion of the arc volcanism, but a higher volcanic output rate is a reasonable proxy for a higher magma production rate because the latter is generally accompanied with the former. Among the volcanic output rates that were determined for a few volcanoes or margin segments of a given subduction zone, we choose one with the longest well-constrained history of activity so that the rate is based on several eruptive cycles and is closest to the long-term average. Figure 3b shows that the rate of arc magma production has a strong tendency to increase with φ.

[20] Although there is some evidence of adiabatic decompression melting of the upwelling mantle [e.g., *Kohut et al.*, 2006], arc magmas are believed to be generated largely by hydration melting, that is, melting due to the reduction of mantle solidus by the addition of fluid into the hot region of the mantle wedge. This view of melt generation is supported by the relatively high water content and enrichment of fluid-mobile elements in arc lavas [*Gaetani and Grove*, 1998; *Pawley and Holloway*, 1993; *Ulmer*, 2001]. The rate of magma production is likely to be strongly influenced by the amount of fluid fluxing from the subducting slab into the overriding mantle. Therefore, the increase in arc magma production with φ may partly due to the greater ability of colder slabs to carry fluids to the subarc depths. In some works, such as *Grove et al.* [2009], great emphasis is placed on the dehydration of mantle wedge material that was hydrated at a slightly shallower depth and then brought down to the subarc depth by wedge flow, but we think that fluid from the dehydrating slab directly beneath the arc is far more important. Region-specific processes such as intra-arc rifting and sediment subduction to the subarc depth are likely to affect magma production and cause large scatter of the magma production rates (Figure 3b).

2.5. Configuration of Subduction Zones: Depth of the Slab Beneath the Volcanic Arc

[21] *England et al.* [2004] determined the depth to the top of intraslab seismicity beneath the arc for twenty-four margin segments using teleseismically determined intraslab earthquake hypocenter locations in the EHB catalog. We use this depth to approximate the subarc slab depth (H). The precise location of the intraslab earthquakes relative to the slab surface in the arc area is poorly known unless extensive seismic data (e.g., waves that are converted at or reflected from the slab surface or that are guided by the subducting crust) allow the detection of the slab surface, such as in NE Japan [e.g., *Zhao et al.*, 1997]. The inference of H from the intraslab seismicity thus results in a tendency to overestimate H, because the shallowest events beneath the arc may actually be in the subducting mantle at some depth from the slab surface. A greater tendency of overestimating H is expected for older and colder slabs, in which intraslab seismicity can occur in a thicker band that extends deeper into the slab away from the slab surface (e.g., Mariana). A greater uncertainty in H is expected for a steeply dipping slab owing to greater sensitivity of H to small changes in the position of the arc and horizontal location of intraslab earthquakes. Other source of uncertainties in H includes uncertainties in earthquake hypocenters.

[22] The values of H determined by *England et al.* [2004] for the twenty-four margin segments range from 65 km to 130 km with the mean of ~100 km. About 54% of them fall in the range of 90–100 km, and 88% of them are in the 80–120 km range, confirming that H is relatively uniform. Similarly, 46% of individual volcanoes used to determine H in the twenty-four margin segments are situated where the slab is in the 90–100 km depth range, and 83% of them are situated where the slab is in the 80–120 km depth range.

[23] *Syracuse and Abers* [2006] determined H for fifty-one margin segments by delineating the slab surface on the basis of the distribution of intraslab earthquakes in the EHB catalog. For the twenty-

four margin segments investigated by *England et al.* [2004], the values of H determined by the two studies are similar (within 20 km) except for Java and Mariana. At these two margin segments, H determined by *Syracuse and Abers* [2006] is deeper than that determined by *England et al.* [2004]. The slab at these margins is relatively old and dips steeply, and the determination of H may be affected by the uncertainties discussed above. *Syracuse and Abers* [2006] also suggested that there might be a need to adjust H to account for errors in hypocenter locations. The adjusted depths (H') are systematically deeper than H (by up to ~40 km).

[24] Besides the above two studies, H has also been determined independently using local seismic networks in some subduction zones. Where the local networks are dense and the slab geometry is relatively simple, the determination of H using the local networks is rather accurate and provides a "calibration" for the teleseismically determined H. At NE Japan, H determined using the very dense local network is ~100 km [e.g., *Nakajima et al.*, 2001]. The depths determined by both *England et al.* [2004] and *Syracuse and Abers* [2006] are also ~100 km while H' is 111 km. In northern Hikurangi, H determined with a similarly dense local network is ~85 km [*Reyners et al.*, 2007]. For the same location, the depths determined by *England et al.* [2004] and *Syracuse and Abers* [2006] are 110 km and 123 km, respectively, and H' is 147 km. The values of H determined by the two studies are in relatively good agreement with the "calibration" values. The adjustment made to produce H' does not appear to improve the deviation from the calibration values, and therefore we use H only in this study.

[25] The H values determined by *England et al.* [2004] for most of the seventeen subduction zones investigated in this study are shown in Figure 3c. Cascadia, Nankai, Mexico, Colombia-Ecuador, SC Chile, and Costa Rica were not included in their study mostly because of the paucity of intraslab seismicity directly beneath the arc. Of these margins, *Syracuse and Abers* [2006] determined H for SC Chile and Costa Rica, and we use their values for these two margins. For Cascadia and Mexico, we use H given by slab geometry models reported in the literature (Table 1). For the other two subduction zones, the slab shape reported in the literature is only for the shallow part of the slab, most of which is based mainly on controlled-source seismic surveys. We extrapolate H from the slab shape at shallow depths with the aid of limited intraslab earthquakes in the EHB catalog. Details of the slab geometry model for individual subduction zones are described in sections 4 and 5 and Appendix A as part of the description of mesh construction for thermal modeling. For northern Hikurangi, we use the value of H determined with the local network, but defining the precise location of the volcanic arc is somewhat problematic because of complications caused by ongoing intra-arc and back-arc rifting.

[26] Figure 3c shows the tendency for the volcanic arc to form where the slab is about 100 km deep. The most striking characteristic of the arc location is its lack of a systematic dependence on φ (Figure 3c), in contrast with other subduction zone processes discussed above. The independence of the arc location on φ is particularly intriguing considering the strong dependence of the intensity of arc volcanism on φ.

[27] By comparing H with a range of subduction parameters, both *England et al.* [2004] and *Syracuse and Abers* [2006] suggest that the kinematics of the subducting slab is at least partly responsible for the small variations in H. However, the first-order question of why the depth tends to be around 100 km is yet to be addressed as mentioned in section 1.

3. Hypothesis of a Common Maximum Depth of Slab-Mantle Decoupling

[28] In section 2, we illustrated by reviewing available observations that many geophysical processes in subduction zones vary systematically with the slab thermal state while the configuration of subduction zones is rather uniform. Here, we propose a possible mechanism that reconciles the two contrasting trends.

[29] Let us first reemphasize the strong thermal contrast between the cold fore arc and hot arc and back arc in subduction zones [*Wada et al.*, 2008]. The most direct evidence of this contrast is surface heat flow: It is low in the fore arc and high in the arc and back arc region. The cold thermal state of the fore-arc mantle is also required for inferred mantle wedge serpentinization (<~700°C) at several subduction zones (section 2.3). The occurrence of earthquakes in the fore-arc mantle wedge (e.g., NE Japan) also indicates a relatively cold thermal condition. In contrast to the cold fore-arc mantle, the subarc mantle is hot, as supported by high

surface heat flow and the generation of melt for arc volcanism. Experimentally determined solidus for H_2O-staurated mantle peridotite at 100 km depth ranges from 800 to 1000°C [e.g., *Schmidt and Poli*, 1998; *Grove et al.*, 2006]. The melting in the mantle wedge is expected to occur at higher temperatures than these estimates since the mantle source is typically not fully saturated with H_2O [e.g., *Ulmer*, 2001]. Geochemical and thermobarometric data on arc lavas and exhumed lower crust and mantle rocks indicate temperatures of 1300–1400°C in the mantle wedge [e.g., *Kelemen et al.*, 2003, and references therein]. These estimates may however be higher than the actual mantle temperatures because of the assumed steady state geotherm for the magma that is likely to be transient. On the basis of these petrological estimates with their uncertainties taken into account and the experimental constraints discussed above, it is widely agreed that mantle temperatures beneath the arc should be greater than 1200°C [*Kelemen et al.*, 2003]. Although melt may migrate laterally because of pressure gradient and fracture distribution, its migration is driven primarily by its positive buoyancy and is thus dominantly upward. Therefore, it is reasonable to assume that the partial melting of the mantle and thus the region of high temperature (>1200°C) occur directly beneath the volcanic arc. The thermal contrast between the fore-arc mantle and subarc mantle is large, and the transition between the two thermal regimes is sharp.

[30] The two most important factors that govern the thermal regime of subduction zones are the thermal state of the subducting plate and the mantle wedge flow. The thermal state of the subducting plate obviously has a first-order impact on various processes as discussed in section 2 (Figures 3a and 3b). However, the thermal effect of the slab cannot be dominant in the region of the volcanic arc, as evidenced by its lack of influence on the location of the arc (Figure 3c). We reason that this is because the thermal effect of the slab is overshadowed by that of the mantle wedge flow in the arc region. As we will further demonstrate using numerical models that the sharp thermal contrast between the cold fore arc and hot arc discussed in the preceding paragraph is due to the sudden onset of mantle wedge flow near the arc. In most of the fore arc, there is no mantle wedge flow, and the thermal regime is controlled mainly by the relatively cold subducting slab whereas in the arc region, the thermal regime is controlled mainly by the mantle wedge flow which brings in much heat from the back arc and greater depths.

[31] What causes the sudden onset of mantle wedge flow near the arc? Flow of the mantle wedge is driven by its viscous coupling with the subducting slab. The cold fore arc indicates the local absence of significant mantle flow, and the necessary condition for a stagnant mantle wedge is that it must be decoupled from the subducting slab [*Wada et al.*, 2008]. Farther down-dip, an increase in the slab-mantle coupling causes a sudden onset of mantle wedge flow and hence the sharp transition from the cold fore-arc mantle to the hot subarc mantle. Therefore, the key parameter to investigate is the maximum depth of slab-mantle decoupling (the MDD). To explain the uniform configuration of subduction zones, we hypothesize that most, if not all, subduction zones share a common MDD. In the following, we test this hypothesis using numerical thermal models.

4. Thermal Models

4.1. Modeling Method

[32] We use a steady state two-dimensional finite element model [*Currie et al.*, 2004; *Wada et al.*, 2008]. Similar to most previous subduction zone thermal models, our model consists of a nondeforming overriding plate, a subducting slab with prescribed motion, and a viscous mantle wedge in which the flow field is to be calculated (Figure 4). We employ a temperature- and stress-dependent wet olivine rheology for the mantle wedge [*Karato and Wu*, 1993; *van Keken et al.*, 2002; *Currie et al.*, 2004; *Wada et al.*, 2008]. The governing equations for the flow and temperature fields are as described by *van Keken et al.* [2002] except for the addition of viscous energy dissipation, and the numerical method is exactly as described by *Currie et al.* [2004]. The flow law and the definition of the effective viscosity used for the mantle wedge are as described by *Wada et al.* [2008]. The dimensions of elements in our model typically range from ~10 m to ~15 km. The model uses nine-node elements for the temperature and velocity fields and compatible four-node elements for the pressure field. The quadratic nine-node elements allow much higher model resolution compared to linear elements of similar sizes. Several other numerical codes with different numerical methods are available for subduction zone thermal modeling. A community benchmarking exercise for these codes, including the one used in this study, shows that

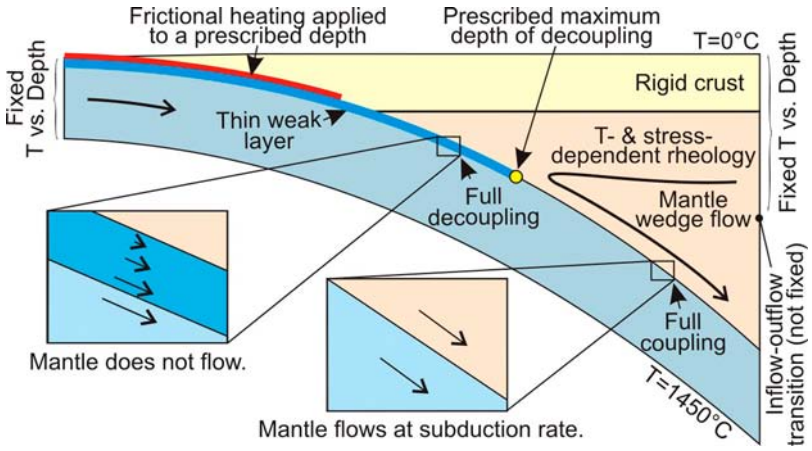

Figure 4. Schematic illustration of boundary and interface conditions for the thermal models. Insets show the velocity field across the decoupled and coupled parts of the interface.

they are in reasonable agreement [*van Keken et al.*, 2008].

[33] In the study of subduction zone thermal structures, mantle wedge flow is commonly modeled as basally driven corner flow induced by kinematically prescribed motion of the subducting slab. To create the two contrasting thermal regimes in the mantle wedge, a rigid wedge corner is imposed to prevent hotter mantle material from entering the corner in some models [*Peacock and Wang*, 1999; *van Keken et al.*, 2002; *Currie et al.*, 2004]. However, the primary factor that controls the vigor of mantle wedge flow is the slab-mantle wedge coupling. Therefore, a free slip condition, reduced velocity, or low stress condition has been prescribed along the shallow part of the slab-mantle wedge interface by some researchers to demonstrate the effect of decoupling on mantle wedge flow and temperatures [e.g., *Furukawa*, 1993; *Kneller et al.*, 2005; *Wada et al.*, 2008].

[34] In this study, following *Wada et al.* [2008], we use a thin layer of low viscosity along the interface, in effect simulating a low stress condition. In the model of *Wada et al.* [2008], the thin layer of a fixed thickness (100 m) extended along the entire length of the slab, and the degree of decoupling was controlled by the layer viscosity. With a realistic temperature- and stress-dependent mantle wedge rheology, the mantle strength decreases with increasing temperature and hence with depth, and decoupling is terminated where the strength contrast disappears. In this case, the downdip length of the thin layer has no effect as long as it extends beyond the temperature-controlled downdip extent of decoupling.

[35] *Wada et al.* [2008] found that the nonlinear feedback between temperature and mantle viscosity always leads to nearly complete stagnation of the mantle wedge above a weakened interface and that the downdip transition from decoupling to coupling along the interface is always sharp. This is because a slight reduction in flow velocity due to a weakened interface leads to lower temperatures because conductive cooling due to the presence of the slab becomes more dominant than convective transfer of heat by wedge flow. The lower temperature causes a higher effective viscosity, leading to an increase in the strength contrast between the mantle wedge and the interface and further decoupling. We further tested the flow behavior by using a dislocation-creep interface layer and found that the bimodal flow behavior and the sharpness of the decoupling-coupling transition are persistent regardless of the rheology or the thickness of the layer. The modeling results are presented elsewhere [*Wada*, 2009]. The complete stagnation of the mantle wedge explains why some earlier thermal models with an imposed no-flow wedge corner [e.g., *Peacock and Wang*, 1999; *Hacker et al.*, 2003; *van Keken et al.*, 2002; *Currie et al.*, 2004] satisfy the observed low surface heat flow in the fore arc. The sharp decoupling-coupling transition allows some simplifications to be made to the model of *Wada et al.* [2008]; the weak interface layer can be truncated at a prescribed depth for numerical convenience with a minimal effect on the mantle wedge flow pattern. Thus, in this study, we truncate the weak interface layer at a prescribed MDD. In this case, the exact value of the viscosity of the interface layer is unimportant as long as it is low enough to cause decoupling. We

use the layer viscosity of 10^{17} Pa s in this study. The MDD itself will be the only variable parameter to be tested in the thermal model.

4.2. Model Geometry and Parameters

[36] For each subduction zone, a model is developed along a representative corridor oriented roughly in the margin-normal direction. The shape of the subducting slab has been reported previously for northern Cascadia, Nankai, Mexico, Kyushu, Alaska, northern Costa Rica, Hikurangi, and NE Japan, and we use the existing slab geometry models for these subduction zones. However, the slab geometry model for Nankai extends only to ~60 km depth, and thus we extrapolate the deeper part of the slab from the existing slab geometry model. For the other subduction zones, we construct a slab geometry model using earthquake locations from the EHB catalog, *H* determined by *England et al.* [2004] and *Syracuse and Abers* [2006], and other available seismological observations reported in the literature. For Colombia-Ecuador and SC Chile, the slab geometry at depths greater than 90 km depth is extrapolated from the shallower part of the slab due to the absence of deeper intraslab seismicity and lack of seismological observations on the slab shape. The references for the slab geometry model and other model parameterization are summarized in Table 3. Details of how the slab geometry was obtained for individual subduction zones are provided with the modeling results in section 5 and Appendix A.

[37] In the thermal model, there is no practical need to differentiate between the subducting crust and mantle. However, in the determination of the metamorphic boundaries in the subducting slab from the thermal modeling results, the subducting crust and mantle need to be differentiated owing to their compositional difference. We assume that the subducting crust has the global average oceanic crustal thickness of 7 km, except for northern Hikurangi where the 17-km thick oceanic Hikurangi Plateau is being subducted [*Davy and Wood*, 1994].

[38] In the model, we assign zero flow velocities to the overriding plate from the surface to its Moho depth. The Moho depth has little effects on mantle wedge flow because the actual base of the "rigid" part of the plate is deeper at a thermally controlled rheological transition. However, the Moho depth at continental convergent margins is relevant to converting depth to pressure when the thermal modeling results are used to determine the metamorphic state of the subducting slab and mantle wedge. Therefore, in the models for continental margins, we assign the thickness of the overriding crust in each model in accordance with the Moho depth reported in published seismological studies (Table 3). We use a conventional approach of using lithostatic pressure in the determination of the depth of phase transformation. Errors due to neglecting dynamic pressure associated with viscous flow in our petrological model are expected to be much smaller than uncertainties in the metamorphic phase boundaries. The Moho depth of the overriding plate at the thirteen continental margins is mostly in the range of 30–40 km except in northern Chile where the thickness of the overriding crust in the fore-arc region is reported to be in the range of 50–70 km [*Yuan et al.*, 2000; *Koulakov et al.*, 2006]. We thus assume a 60-km-thick crust for the northern Chile model. For the calculation of pressure, we assume a uniform density of 2750 kg/m^3 for the overriding continental crust and 3300 kg/m^3 for the mantle wedge and the subducting slab.

[39] At ocean-ocean margins, the overriding crust consists primarily of mafic material, and thus we assume the same density for the overriding crust as for the mantle wedge. We use the global average oceanic crust thickness of 7 km for the overriding crust at ocean-ocean margin. The thickness of the overriding oceanic crust in the arc–fore-arc region can be slightly thicker than 7 km as reported by seismic studies in Izu-Bonin-Mariana margin [e.g., *Kodaira et al.*, 2007], and thus the actual mantle wedge at some ocean-ocean margins may not extend to depths as shallow as portrayed in some of our models for this type of margins.

[40] We use typical values of thermal conductivity and radiogenic heat production rates for the continental crust, subducting crust, and mantle deduced from field measurements and laboratory data (Table 4). However, in northern Cascadia, where very detailed thermal measurements have been made, the overriding upper crustal material in the fore-arc region is composed of mafic material and contains significantly less amounts of radiogenic elements than average continental material [*Lewis et al.*, 1988]. Therefore, in the northern Cascadia model, we use lower radiogenic heat production rates in the fore-arc crust, which increases from zero at the deformation front to a typical continental rate near the arc [*Wang et al.*, 1995]. Following *van Keken et al.* [2002], we assume a constant specific heat of 1250 J/kg K.

Table 3. Summary of Model Parameterization

Index	Subduction Zone	Intersection of Model Profile and Trench		Profile Direction[a] (deg)	References for Slab Geometry Model[b]	Trench Depth (km)	Sediment Thickness (km)	References for Sediment Thickness	Crustal Thickness (km)	Downdip End of Frictional Heating (km)	Back-Arc Heat Flow (mW/m^3)
		Long. (deg)	Lat. (deg)								
1	N. Cascadia	−126.3	47.8	62	*McCrory et al.* [2004]	2	3	*Davis and Hyndman* [1989]	35	15	75[c]
2	Nankai	134.5	32.2	331	*Wang et al.* [2004], *Shiomi et al.* [2004]	4	2	*Clift and Vannucchi* [2004]	35	25	69[c]
3	Mexico	−103.3	17.55	30	*Currie et al.* [2002]	5			40	30	72[c]
4	Colombia-Ecuador	−79.8	2.4	125	*Marcaillou et al.* [2006, 2008], *Engdahl et al.* [1998]	3	4	*Marcaillou et al.* [2006, 2008]	40	30	80[d]
5	SC Chile	−74.7	−38.1	106	*Groß et al.* [2008], *Syracuse and Abers* [2006], *Engdahl et al.* [1998]	5	2	*Groß et al.* [2008]	40	40	80[d]
6	Kyushu	132.5	30.8	296	*Wang et al.* [2004], *Baba et al.* [2002]	4	2	*Clift and Vannucchi* [2004]	30	30	69[c]
7	N. Sumatra	97.1	−0.5	54	*Engdahl et al.* [1998], *England et al.* [2004]	5	2.5	*Clift and Vannucchi* [2004]	30	30	120[e]
8	Alaska	−148.2	57.3	309	*Oleskevich et al.* [1999]	4	2.5	*Clift and Vannucchi* [2004]	40	40	80[d]
9	N. Chile	−71.3	−23.5	90	*Sallarès and Ranero* [2005], *Engdahl et al.* [1998], *England et al.* [2004]	8			60	35	85[c]
10	N. Costa Rica	−86.3	9.7	42	*Peacock et al.* [2005], *Syracuse and Abers* [2006]	5			30	30	80[d]
11	Aleutians	−179.7	50.2	0	*Engdahl et al.* [1998], *England et al.* [2004]	5	1.5	*Clift and Vannucchi* [2004]	10	20	75[c]
12	N. Hikurangi	179.2	−40.0	310	*Reyners et al.* [2006]	2.7			30	10	80[d]
13	Mariana	147.9	17.9	270	*Engdahl et al.* [1998], *England et al.* [2004]	8			10	20	80[d]
14	Kermadec	−176.2	−29.3	289	*Engdahl et al.* [1998], *England et al.* [2004]	7.5			10	20	80[d]
15	Kamchatka	161.3	51.7	300	*Engdahl et al.* [1998], *England et al.* [2004]	8			30	40	70[c]

Table 3. (continued)

Index	Subduction Zone	Intersection of Model Profile and Trench		Profile Direction[a] (deg)	References for Slab Geometry Model[b]	Trench Depth (km)	Sediment Thickness (km)	References for Sediment Thickness	Crustal Thickness (km)	Downdip End of Frictional Heating (km)	Back-Arc Heat Flow (mW/m^3)
		Long. (deg)	Lat. (deg)								
16	Izu	142.3	31.4	263	*Engdahl et al.* [1998], *England et al.* [2004]	10			10	20	80[d]
17	NE Japan	143.3	36.8	293	*Hasegawa et al.* [1994], *Nakajima et al.* [2001], *Takahashi et al.* [2007], *Zhao et al.* [1994]	8			30	40	88[c]

[a] The profile direction is measured from north.
[b] Slab geometry at >60 km depths in Nankai and at >90 km depths in Colombia-Ecuador is extrapolated from the slab geometry model for the shallow part of the slab.
[c] The value is the regional average back-arc surface heat flow value of the corresponding subduction zone [*Currie and Hyndman*, 2006].
[d] The value is the global average back-arc surface heat flow [*Currie and Hyndman*, 2006].
[e] The value is the regional average back-arc surface heat flow value obtained from GHFD.

4.3. Boundary Conditions

[41] Following *Peacock and Wang* [1999], we assign constant temperatures of 0°C and 1450°C to the upper and lower boundaries of the model, respectively. To the trenchside vertical boundary, we prescribe a geotherm calculated by using the GDH1 plate cooling model [*Stein and Stein*, 1992] for an appropriate slab age in most of our models. However, at northern Cascadia, Nankai, Colombia-Ecuador, SC Chile, Kyushu, northern Sumatra, Alaska, and Aleutians, the incoming plate is blanketed by a thick (>1 km) sediment cover, which increases the temperature of the top part of the plate. Although the effect of this increased temperature on the deeper part of the subduction zone is expected to be small, we include the thermal effects of sediment deposition and compaction when calculating the oceanic plate geotherm for these margins by using a time-dependent 1-D finite element code of *Wang and Davis* [1992]. We assume conservative sedimentation rates of ~1 mm/yr and let the sediment accumulate to the present thickness (Table 3) at the trench. The thermal models do not feature sediment subduction because its thermal effect is negligibly small. The thermal effects of hydrothermal circulation in the top 1–2 km of the incoming oceanic crust are limited within ~20 km distance arcward of the trench [*Harris and Wang*, 2002]. Hydrothermal circulation in the crust may continue after subduction, but its cooling effect at depth is small (<50°C) unless vigorous hydrothermal circulation continues to a great depth (>15 km) [*Spinelli and Wang*, 2008]. Therefore, we neglect the effects of hydrothermal circulation in our models.

[42] At many subduction zones, isochrons on the incoming plate are subparallel to the trench, and the age of the plate at the trench is relatively constant with time as assumed in our steady state models. However, at subduction zones with nearly margin-normal isochrons, the incoming plate at the

Table 4. Thermal Properties Used in the Models

Property	Material	Value
Thermal conductivity (W/mK)	continental crust	2.5
	mantle and oceanic crust	3.1
Heat generation (μW/m^3)	continental upper crust	1.3[a]
	continental lower crust	0.4
	mantle and oceanic crust	0.02

[a] Values of 0–1.3 are used for northern Cascadia.

trench becomes older and thus cooler with time. The effect of neglecting this time dependence of the thermal state of the incoming plate in our steady state models is insignificant for old slabs. However, for young slabs such as in Nankai and Colombia-Ecuador where the isochrons are nearly margin-normal, the models of constant slab age determined by using the isochron presently at the trench predict a thermal state slightly colder than actual.

[43] For the shallow part (<∼60 km depth) of the back-arc-side vertical boundary, we use a conductive heat equation to calculate the geotherm. We calculate the geotherm to give the back-arc surface heat flow value reported by *Currie and Hyndman* [2006] for northern Cascadia, Nankai, Kyushu, Mexico, Alaska, Aleutians, Kamchatka and NE Japan. For northern Sumatra, the continental geotherm is calculated to fit the dense back-arc heat flow data in Global Heat Flow Database (GHFD) (The global heat flow database of the International Heat Flow Commission, The International Heat Flow Commission of the International Association of Seismology and Physics of the Earth's Interior, http://www.heatflow.und.edu/index2.html; last updated 10 August 2008), which indicate unusually high heat flow of ∼120 mW/m^2. This high heat flow may indicate high crustal radiogenic heat production or hydrothermal processes in the region [*Hippchen and Hyndman*, 2008]. For the rest, where there is no direct observational constraint, we applied the global average back-arc heat flow of 80 mW/m^2 as concluded by *Currie and Hyndman* [2006]. After a number of tests, however, we found that the assumed back-arc surface heat flow has little effect on the fore-arc–arc mantle wedge thermal structure unless it is unreasonably low (<∼50 mW/m^2) because the heat supply from the back-arc to the fore-arc–arc region is controlled by the geotherm of the deeper flowing part of the back arc to be discussed in the following paragraph.

[44] We assign a geotherm calculated by using an adiabatic gradient of 0.3°C/km and a mantle potential temperature of 1295°C [*Ito and Katsura*, 1989] for the deeper part of the back-arc-side boundary. In theory, the use of an adiabatic temperature gradient along this boundary is inconsistent with the assumption of the Boussinesq flow. We allow this inconsistency in order to curb the nonlinearity of the problem and thus to simplify the model, as is commonly practiced in subduction zone thermal modeling. The effect of this simplification on the flow and thermal fields in the shallow part (<∼200-km depth) of the mantle wedge is very small [e.g., *Lee and King*, 2009]. The application of the adiabatic temperature gradient compensates for the missing effect of adiabatic heating in the model and therefore provides a good compromise. The adiabatic gradient is meant to represent vigorous mantle convection (buoyancy-driven flow) in the back-arc region that supplies heat to the fore-arc–arc mantle wedge [*Currie et al.*, 2004; *Currie and Hyndman*, 2006; *Wada et al.*, 2008]. In the fore arc, buoyancy-driven flow is discouraged because of the diminishing vertical dimension of the mantle wedge and relatively small temperature difference between its top and bottom. The transition between the buoyancy-driven and slab-driven flow regimes must take place somewhere in the back-arc region near the arc. We simulate only the slab-driven mantle flow in the fore-arc and arc regions, and the back-arc-side boundary must be placed at a short distance landward of the arc. The location of this boundary has a small effect on the temperatures of mantle material flowing into the model domain, and a horizontal shift by ∼50 km causes up to ∼20°C difference in the subarc mantle temperature. For consistency, we place the boundary at 150-km horizontal distance from the point of MDD in all models. For given heat supply from the back-arc and mantle rheology, mantle temperature in the fore-arc–arc region depends primarily on the mantle wedge flow pattern, which is controlled by the MDD and the kinematics of the slab (subduction rate and slab dip) as will be shown in section 5.

4.4. Frictional and Shear Heating

[45] We apply frictional heating along the interface from the surface to near the depth of the downdip limit of the seismogenic zone that is estimated by other studies (Table 3). Frictional heating is the product of fault slip rate and shear stress $\tau = \mu'\sigma_n$, where μ' is the effective coefficient of friction and σ_n is normal stress, which is approximated by the weight of the overlying rock column in our model. Seismological and field observations [e.g., *Magee and Zoback*, 1993], frictional heating studies along subduction faults [e.g., *Wang et al.*, 1995; *von Herzen et al.*, 2001], and mechanical models for the fore-arc stress state [e.g., *Wang and He*, 1999; *Wang and Suyehiro*, 1999] indicate that the temporally and spatially averaged effective coefficient of friction of subduction faults is usually no greater than 0.05, and in this study, we assume $\mu' = 0.03$. We apply viscous heating along the ductile part of

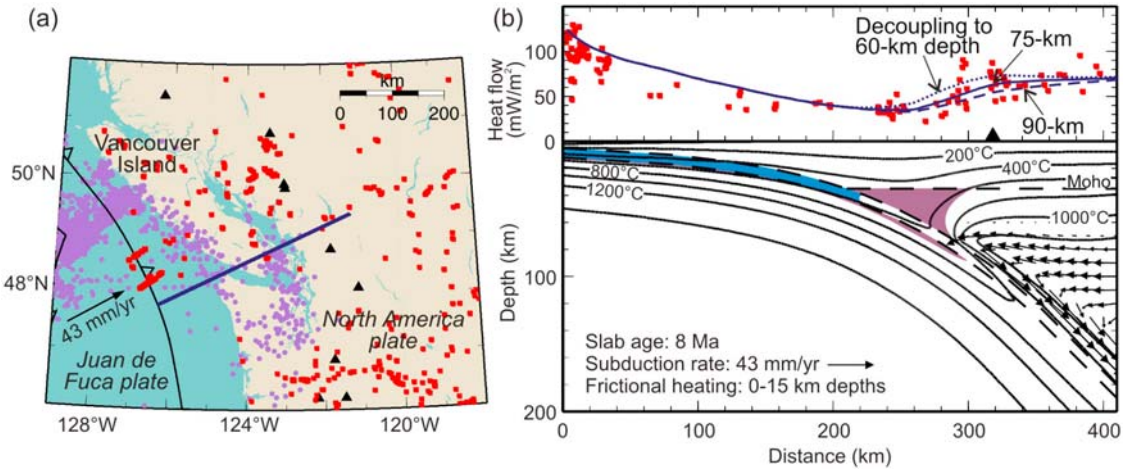

Figure 5. (a) Map of northern Cascadia (index number 1), showing the distributions of surface heat flow observations (red squares) and earthquakes in the Juan de Fuca plate (purple dots). The blue thick line indicates the profile line for the northern Cascadia thermal model. (b) Observed (red squares) and model-predicted (blue lines) surface heat flows and model-predicted flow and temperature fields with the 75-km maximum depth of decoupling for northern Cascadia. Surface heat flow measurements [*Currie et al.*, 2004; *Wang et al.*, 1995] within 100 km of the profile line are plotted in Figure 5b. The scatter of heat flow values near the volcanic arc is caused by local near-surface processes. Arrows in the mantle wedge indicate flow velocities. Blue and white in the subducting crust represent regions of high (0.7–5.4 wt.%) and low (≤0.7 wt.%) H_2O contents, respectively [*Hacker et al.*, 2003]. The boundary between them roughly represents the basalt-eclogite transformation under thermodynamic equilibrium, which releases a large amount of H_2O. The transformation may be kinetically delayed in the lower subducting crust. Purple in the mantle wedge and slab mantle indicates zones of antigorite stability [*Schmidt and Poli*, 1998]. We adopted the slab geometry model of *McCrory et al.* [2004], which was constructed for Cascadia by using intraslab earthquakes, seismic reflection and refraction data (<50 km depth), and tomographic images of seismic velocity structures obtained from teleseismic studies for the deeper part. The model slightly overpredicts offshore heat flow because the slab in the model, intended to represent a northern Cascadia average, dips more shallowly than central Vancouver Island, where most of the heat flow data were obtained, but this has little effect on the mantle wedge thermal structure.

the subduction interface and in the mantle wedge. The rate of viscous heating is calculated from the product of shear stress and shear strain rate (the second invariants of the stress and strain rate tensors).

5. Thermal Modeling Results

5.1. Maximum Depth of Decoupling Consistent With Surface Heat Flow Data: Northern Cascadia and NE Japan

[46] We first consider models for two subduction zones that have extensive heat flow constraints, northern Cascadia and NE Japan (Figures 5 and 6, respectively). They happen to represent end-member warm- and cold-slab subduction zones: northern Cascadia has a very young (~8 Ma) and warm slab whereas NE Japan has a very old (~130 Ma) and cold slab. They show dramatic contrasts in their metamorphic, volcanic, and seismological characteristics, but they have a similar configuration in that the volcanic arc is located where the slab is about 100 km deep (Figure 3). Heat flow measurements near the trench at these two margins reflect the ages of the subducting plates, but in both places, values are low in the rest of the fore arc until some 20–50 km trenchward of the volcanic arc. Limited heat flow data from other subduction zones are also consistent with this pattern (Appendix A).

[47] We first prescribed the MDD at various depths in the northern Cascadia and NE Japan models to investigate the variation in the mantle wedge thermal structure and surface heat flow patterns. The downdip transition from decoupling to coupling has a dramatic effect on the flow pattern and thermal regime of the mantle wedge. The mantle wedge is stagnant over the decoupled part of the interface but flows at full speed over the coupled part as controlled by the slab velocity and mantle

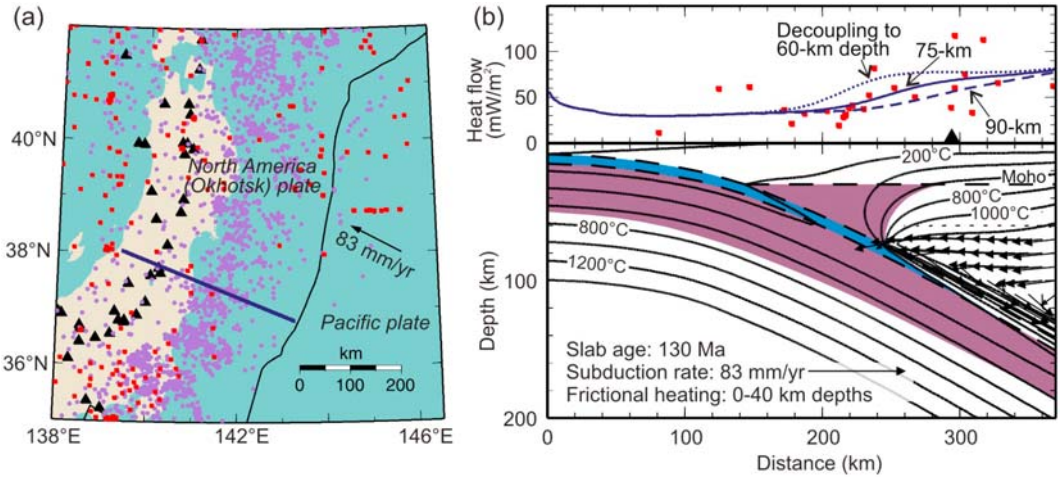

Figure 6. (a) Map and (b) modeling results with 75-km maximum depth of decoupling for NE Japan (index number 17) presented in the same way as Figure 5. Surface heat flow measurements [*Tanaka et al.*, 2004] within 200 km of the profile line are plotted in Figure 6b. We use the slab geometry model that has been constrained by numerous studies using intraslab seismicity, seismic reflection and refraction data, and tomographic images of seismic velocity structures [*Nakajima et al.*, 2001; *Takahashi et al.*, 2007; *Hasegawa et al.*, 1994; *Zhao et al.*, 1994].

rheology. The stagnant part is cold because of conductive cooling caused by the descending slab, resulting in low surface heat flow. The flowing part is hot because the wedge flow brings in heat from greater depths and the back arc, resulting in high surface heat flow. The thermal contrast between the cold and the hot part of the mantle wedge is sharp, and the transition from low to high surface heat flow values is governed by the downdip termination of the decoupled interface.

[48] An MDD of ~75 km can explain the heat flow data at both northern Cascadia and NE Japan (Figures 5 and 6, respectively), consistent with the modeling results of previous studies [e.g., *Furukawa*, 1993; *Wada et al.*, 2008]. Increasing or decreasing the MDD by 15 km will lead to a poorer fit between the model-predicted and observed surface heat flow patterns, and in both cases, a deeper MDD (e.g., 90 km) results in a subarc mantle wedge temperature that is too low (<1200°C) for melt generation.

[49] The model-predicted depths of basalt-eclogite transformation which roughly corresponds to the peak crustal dehydration in the subducting crust are 40–47 km in the young slab in Cascadia but 75–140 km in the old slab in NE Japan. The greater depth for NE Japan is due to the cooler thermal state of the slab, and the large depth range is due to the steep Clapeyron slope (dP/dT) of the basalt-eclogite transformation over the temperature range of the subducting crust [*Hacker et al.*, 2003]. The predicted depths of the basalt-eclogite transformation are consistent with the downdip extent of an LVL at 45–75 km depths and 100–150 km depths reported for northern Cascadia and NE Japan, respectively (Figure 3a). The slightly deeper extent of the observed LVL may indicate kinetic delay in the transformation of the anhydrous gabbroic lower crust [*Hacker et al.*, 2003]. The model-predicted zone of antigorite stability in the subducting mantle extends to 90 km depth in Cascadia and ~290 km depth in NE Japan (Table 5). The large difference is consistent with the observed difference in the depth ranges of intermediate-depth intraslab seismicity between these two subduction zones (Figure 3a) and supports the hypothesis that the dehydration of antigorite triggers embrittlement and intraslab seismicity in the subducting mantle as proposed by other workers [e.g., *Seno and Yamanaka*, 1996; *Peacock*, 2001; *Brudzinski et al.*, 2007]. The shallow dehydration of the subducting slab in Cascadia provides ample fluid beneath the cold stagnant part of the forearc mantle wedge, promoting mantle wedge serpentinization, while it provides little fluid beneath the arc region for melt generation. The situation is the opposite in NE Japan, for which peak slab dehydration is predicted to occur at greater depths beneath the arc region. These model predictions are consistent with the inferred degree of serpentinization and the observed intensity of arc volcanism for the two subduction zones as summarized in section 2.

Table 5. Summary of Modeling Results

Index	Subduction Zone	Model-Predicted Max Subarc Temperature (°C)	Model-Predicted Depths of Peak Crustal Dehydration (Top, Bottom)[a] (km)	Model-Predicted Max Depth of Antigorite Stability in the Subducting Mantle (km)
1	N. Cascadia	1250	40, 46.5	90
2	Nankai	1260	55, 46	115
3	Mexico	1310	68, 75	130
4	Colombia-Ecuador	1305	63, 65	125
5	SC Chile	1220	72, 93	170
6	Kyushu	1290	71.5, 93	185
7	N. Sumatra	1305	72.5, 92	175
8	Alaska	1215	71.5, 93	195
9	N. Chile	1320	73, 103	210[b]
10	N. Costa Rica	1280	73.5, 121.5	215
11	Aleutians	1250	74, 126	240
12	N. Hikurangi	1120 and 1310[c]	73, 139	220
13	Mariana	1250	74, 117	240
14	Kermadec	1240	74, 141.5	275
15	Kamchatka	1290	74, 126	280[b]
16	Izu	1300	74.8, 132	270[b]
17	NE Japan	1310	75, 139.5	290[b]

[a] The two values shown are the depths of peak crustal dehydration at the top and bottom of the subducting crust, respectively.
[b] The downdip end of antigorite stability is extrapolated beyond the model domain from the modeling results.
[c] The two values are the model-predicted maximum mantle temperatures beneath the oceanside and landside ends, respectively, of the ~40-km-wide Taupo Volcanic Zone.

[50] The models explain not only the differences between the two subduction zones but also their similar subduction zone configuration. In both the Cascadia and NE Japan models, high temperatures (>1200°C) occur in the mantle wedge where the depth of the slab is about 100 km or greater, providing the necessary thermal condition for melt generation beneath the arc but not in the fore-arc region. The thermal models for these two end-member warm- and cold-slab subduction zones indicate that their differences and the intriguing similarity in their subduction zone configuration can be reconciled if the slab-mantle wedge is decoupled to 70- to 80-km depths.

5.2. Common Maximum Depth of Decoupling and Uniform Subduction Zone Configuration

[51] Northern Cascadia and NE Japan have a similar MDD despite their large differences in subduction parameters, supporting our hypothesis that the common maximum MDD can reconcile the uniformity and diversity of subduction zones. To further test this hypothesis, we developed thermal models for the other fifteen subduction zones assuming a common MDD of 75 km and using the same modeling strategy. Limited heat flow observations from these subduction zones provide some model constraints. For example, the model for Kamchatka (Figure 7) shows that the MDD of around 75 km can explain the surface heat flow while providing predictions for the thermal, petrological, and seismological processes that are consistent with the observations. The description of the slab geometry and modeling results for the other fourteen subduction zones are presented in Appendix A except for Mariana, which will be presented in section 5.3.

[52] The models explain why arc volcanism does not occur in the fore arc. In the models of all the seventeen subduction zones, the mantle beneath the arc is flowing and hot, with the temperature exceeding 1200°C, consistent with the thermal condition required for melt generation (Figure 8). Because the ascent of melt does not necessarily follow a strictly vertical path, the source region of melt may not be directly beneath the arc, and the model-predicted subarc mantle temperature may deviate slightly from the actual temperature of the melt source region. Furthermore, the exact thermal condition of mantle melting depends strongly on fluid content. A relatively wide range of subarc mantle temperature predicted by the models is consistent with laboratory predictions and theoretical expectations.

[53] In contrast to the flowing and hot mantle beneath the arc, the stagnant mantle wedge in most

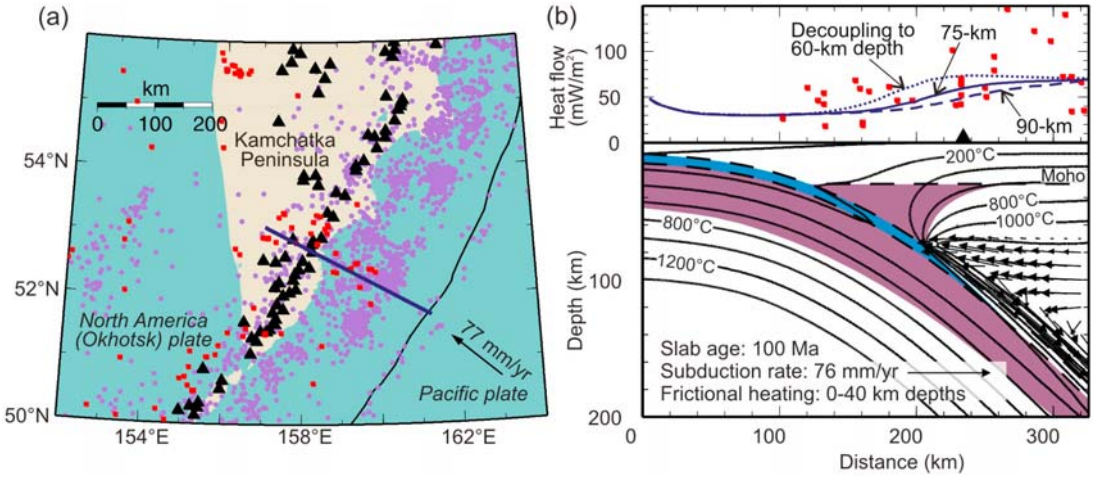

Figure 7. (a) Map and (b) modeling results with 75-km maximum depth for Kamchatka (index number 15) presented in the same way as Figure 5. Surface heat flow measurements [*Tanaka et al.*, 2004] within 100 km of the profile line are projected onto Figure 7b. The slab geometry was obtained in this study using earthquake hypocenters in the EHB catalog and the subarc slab depths determined by *England et al.* [2004].

of the fore arc is rather cold and does not provide the thermal condition for volcanism. Odd volcanoes occasionally occur in the fore arc, such as Mt. St. Helen in Cascadia which is situated ~35 km seaward of the rest of the Cascade volcanoes, but these volcanoes are extremely rare and may be explained by an inclined path of the ascending magma controlled by site-specific geological structures. Furthermore, such volcanism may produce lavas that are geochemically different from those produced in the volcanic arc, enticing alternative explanations [*Defant and Drummond*, 1993].

[54] The models also explain why arc volcanism is difficult to occur in the back arc. As discussed in section 2.4, the generation of melts for arc volcanism requires both high temperature and sufficient fluid supply from the dehydrating slab. The model-predicted depths of peak crustal dehydration and maximum depth of antigorite stability in the subducting mantle for the 17 subduction zone are summarized in Table 5 and Figure 9. The models for all the subduction zones predict that the temperature of the upper part of the subducting slab increases abruptly downdip from the MDD where it is in contact with the overriding flowing hot mantle. Because of this temperature increase, crustal dehydration in all slabs peaks at depths shallower than ~140-km depth and provide little fluid for arc volcanism downdip of this depth. The overlap of the regions of high temperature and high fluid supply by the dehydrating crust occurs in a narrow zone, especially for subduction zones with a steeply dipping slab (e.g., Mariana). In some subduction zones such as NE Japan and Kamchatka, volcanoes are present almost 100 km landward of the volcanic arc. The relatively wide zone of volcanism may partly be attributed to a shallow dip of the slab, but it can be explained by the deeper transportation of fluid by the subducting mantle. The modeling results for cold-slab subduction zones predict that the dehydration of antigorite in the subducting mantle continues to yield fluid beyond ~140 km depth. However, the rate of the fluid supply in general must be much lower because hydration of the mantle lithosphere prior to subduction is likely to be limited to very few deep-cutting faults and also because the zone of antigorite stability shrinks very slowly as the slab travels to greater depths (e.g., Figure 6). The low supply of fluid from the slab downdip of ~140 km

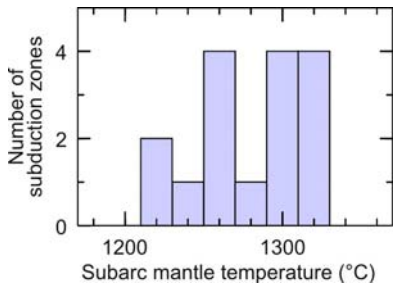

Figure 8. The distribution of the maximum mantle temperature beneath the regional average location of the volcanic arc predicted for all subduction zones with the 75-km maximum depth of decoupling except northern Hikurangi, where ongoing continental rifting makes it difficult to pinpoint the location of the arc.

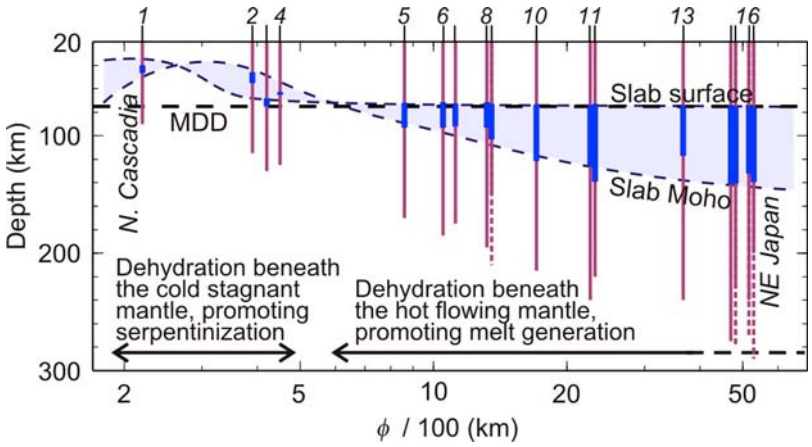

Figure 9. The depth range of peak crustal dehydration (blue lines) predicted by thermal models of the seventeen subduction zones plotted against φ. Light blue area shows the trend of this depth range. The initial decrease in the peak crustal dehydration depth with increasing φ is due to the decrease in the basalt-eclogite transformation depth with decreasing temperature at low pressures. Depth range of antigorite stability in the subducting mantle below 20-km depth is shown with purple lines. Dashed purple lines indicate the portion of the depth range of antigorite stability that is extrapolated beyond the model domain from the modeling results. Small vertical bars and numbers at the top indicate the φ values and index numbers, respectively, of subduction zones.

depth may explain why arc volcanism does not extend much farther landward than observed.

[55] Models with a common MDD explain not only the similarity of H (Figure 3c) but also some important second-order characteristics of these depths, that is, the small variation in H. Faster subduction increases the velocity of mantle wedge flow, which transports heat from the back arc at a faster rate (Figure 10b). This brings the region of high temperatures and thus the volcanic arc slightly closer to the trench, resulting in a smaller H. A steeper slab causes the streamlines of the wedge flow to be oriented more vertically and more effectively transports heat from greater

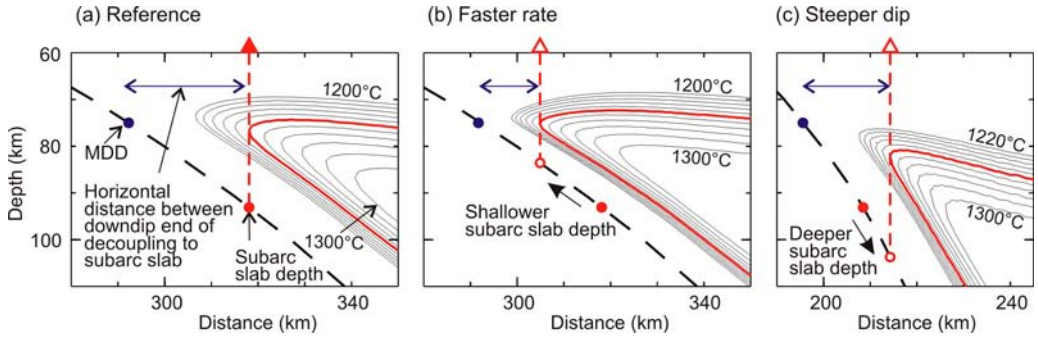

Figure 10. Generic subduction zone thermal models, illustrating the effects of subduction rate and slab dip on the thermally expected location of the volcanic arc and subarc slab depth. Temperature contours between 1200°C and 1300°C at 10°C interval in the flowing part of the mantle wedge calculated by using (a) the northern Cascadia slab geometry and a 43 mm/yr subduction rate, (b) the northern Cascadia slab geometry and a 86 mm/yr subduction rate, and (c) the Mariana slab geometry with a 43 mm/yr subduction rate. The MDD is 75 km (filled blue circle) and the slab age is 8 Ma for all three models. The red contour line indicates 1250°C, which is the model-predicted maximum subarc mantle temperature in northern Cascadia. The filled red triangle and circle are the location of arc and the subarc slab depth, respectively, in northern Cascadia. The horizontal distance (blue line with a double arrowhead) between the downdip end of the decoupled interface and the most seaward point of the 1250°C contour, where melts are expected to be generated, is shorter for a faster subduction rate as shown in Figure 10b or for a steeper slab dip as shown in Figure 10c. The shorter distance means that the arc is located closer to the trench. The predicted subarc slab depth (open red circle) is shallower for a faster subduction rate and deeper for a steeper slab.

depths (Figure 10c). This also brings the arc closer to the trench, but H is deeper because the geometrical effect of a steeper dip on the H overshadows that of the trenchward shift of the arc (Figure 10c). The variations in the subduction rate and slab dip thus can generate the observed range (±∼20 km) of variation in H. This is consistent with the hypothesis that the kinematics of the subducting slab controls the mantle wedge flow pattern and thus the region of melt generation as proposed by *England et al.* [2004] and *Syracuse and Abers* [2006]. For example, the model-predicted dependence of H on the convergence rate and slab dip is consistent with the trends observed along the margins of Kamchatka through Marianas shown in Figure 3 of *Syracuse and Abers* [2006]. Statistical correlations of observed H values with the subduction rate and slab dip are difficult to assess because of the coexistence of the effects of the two parameters and errors in H. For example, *England et al.* [2004] and *Syracuse and Abers* [2006] obtained opposite effects of the slab dip on H or H', respectively.

[56] Although the majority of the H values are in the 80–120 km depth range and their variation is consistent with the common MDD hypothesis, anomalous values of H observed in few subduction zones require further explanation. End-member small and large H values of 65 km and 130 km are reported for eastern Aleutians and Izu, respectively, by *England et al.* [2004]. The steeply dipping slab in eastern Aleutians results in a high sensitivity of H to the arc location, and the very old slab in Izu may generate intraslab earthquakes away from the slab surface, increasing the uncertainties in H as discussed in section 2.5. Furthermore, lateral melt migration may occur, for example, because of the effect of solid-state mantle wedge flow [e.g., *Cagnioncle et al.*, 2007] and can affect the location of arc relative to the region of melt generation and thus H. Alternatively, anomalous subduction zone configuration may be caused by temporal changes in the regional tectonics or slab geometry.

5.3. Common Maximum Depth of Decoupling and Variations of Geophysical Processes With Slab Thermal Parameter

[57] In section 5.2, we demonstrated that the common MDD can explain the uniform configuration of subduction zones. The remaining question is whether this common MDD can also explain the strong slab-age dependent variability of the various observations reviewed in section 2.

[58] The results summarized in Figure 9 demonstrate that the maximum depths of peak crustal dehydration and serpentine stability in the subducting mantle increase systematically with φ. These trends explain the observed variability of the downdip extent of an LVL, which is interpreted to represent untransformed subducting crust (Figure 3a). An LVL detected in the cold-slab Aleutian, Kamchatka, Mariana, and NE Japan subduction zones by *Abers* [2005] extends to greater depths (>∼150 km depths) than the model-predicted depths of basalt-eclogite transformation (<140 km). There are a few possible explanations for this. One is that the transformation in the gabbroic crust is kinetically delayed as mentioned in section 5.1. Another possible explanation is the presence of hydrous minerals, particularly, serpentine, or free fluid in the subducting crust. For example, relatively low seismic velocities observed in the gabbroic oceanic lower crust formed at fast to intermediate-rate spreading centers is explained by alteration of olivine (∼11%) to talc and/or serpentine [*Carlson et al.*, 2009]. After subduction, these hydrous minerals in the lower crust may persist to greater depths than the depths of basalt-eclogite transformation in the upper crust, causing low seismic velocity in the slab. Another possible explanation is that the deeper part of the LVL belongs to the mantle wedge or subducting mantle. For example, in NE Japan, *Kawakatsu and Watada* [2007] also identified an LVL at 140–190 km depths, in the similar depth range to *Abers* [2005], but they showed the layer to be in the mantle above the subducting slab. On the basis of a thermal model assuming an isoviscous mantle wedge, *Kawakatsu and Watada* [2007] interpreted this LVL to be serpentinite. Our models, as well as other thermal models that also incorporate the more realistic temperature-dependent mantle rheology [e.g., *van Keken et al.*, 2002; *Kneller et al.*, 2005], do not predict serpentine to be stable at these depths. We think the LVL may represent the presence of melt that is redistributed along the zone of severe shear deformation immediately above the slab.

[59] The trend shown in Figure 9 also explains the depth range of intraslab seismicity and supports the hypothesis of dehydration embrittlement in both the subducting crust and mantle. Intraslab seismicity extends deeper than the model-predicted downdip extent of antigorite stability in very old cold slabs. This may be due to the replacement of antigorite that survives to ∼200 km depth by phase A, which contains 11.8 wt.% H_2O and is stable to

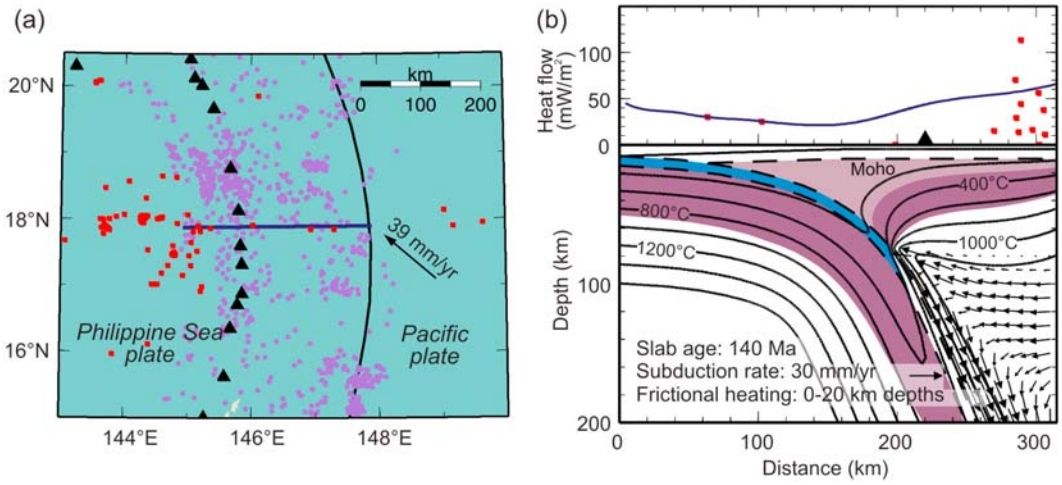

Figure 11. Modeling results for Mariana (index number 13), showing that the shallow part of the mantle wedge at ocean-ocean margins provides a stable thermal condition for low-temperature serpentine species chrysotile and lizardite (light purple). (a) Map and (b) modeling results with 75-km maximum depth of decoupling for Mariana presented in the same way as Figure 5. Surface heat flow measurements (GHFD) within 100 km of the profile line are projected onto Figure 11b. The slab geometry was obtained in this study using earthquake hypocenters in the EHB catalog and the subarc slab depths determined by *England et al.* [2004].

higher temperature than antigorite [*Schmidt and Poli*, 1998].

[60] Our modeling results show that in all the seventeen subduction zones, the stagnant and cold mantle wedge overlying the decoupled part of the interface is in a stable thermal condition to form serpentinites. However, serpentinization depends also on the availability of fluid. The shallow peak crustal dehydration beneath the mantle wedge corner in warm-slab subduction zones provides substantially greater fluid supply than in cold-slab subduction zones where the peak crustal dehydration takes place at greater depths beneath the hot flowing part of the mantle wedge. This model-prediction is consistent with the relatively high degree of mantle wedge serpentinization reported for warm-slab subduction zones and a minor degree of serpentinization in subduction zones with very old and cold slabs except at ocean-ocean margins. At ocean-ocean subduction zones, the mantle wedge overlies the subducting slab at very shallow depths because the overriding oceanic crust is only 7–10 km thick. At these depths in the mantle wedge, lower-temperature serpentine species chrysotile and lizardite can be stable as shown by the modeling results for Marinas (Figure 11) and other three ocean-ocean margins, Aleutians, Kermadec, and Izu (Appendix A). Furthermore, although there is little supply of metamorphic fluid from cold slabs at shallow depths, the collapse of pore space in the subducting sediments and crust provides fluid to serpentinize the shallow-lying mantle wedge. In fact, a high degree of mantle wedge serpentinization at the Izu-Bonin-Mariana margin is evidenced by the formation of serpentine mud volcanism in the fore arc and inferred from seismic observations [*Kamimura et al.*, 2002]. This explains the presence of a highly serpentinized mantle wedge in cold-slab ocean-ocean subduction zones.

[61] At two warm-slab subduction zones, Cascadia and Nankai, the shallow dehydration of the slab over the history of subduction may provide sufficient fluid to cause complete serpentinization of the very tip of the mantle wedge. The continuing dehydration of the subducting slab is likely to result in the accumulation of free fluid near the mantle wedge tip. The presence of free fluid around the mantle wedge tip of these two subduction zones is also inferred from geophysical observations such as low Vs, high Vp/Vs ratio, and high electrical conductivity with strong reflectors [*Kao et al.*, 2005; *Shelly et al.*, 2006], supporting the association of ETS with the presence of free fluid.

[62] The shallow dehydration of warm slabs reduces the downdip transport of fluid to the subarc depth, explaining the feeble arc volcanism. However, arc volcanism does occur in warm-slab subduction zones, and therefore some fluid must be transported to the subarc depth. Possible mechanisms of deep downdip fluid transfer include the subducting lower crust and mantle that contain hydrous minerals such

as antigorite, talc, and chlorite, and the downdip transport of hydrated overriding mantle material by mantle wedge flow. Deeper dehydration of cold slabs provides significantly greater fluid supply for melt production beneath the arc, resulting in intense arc volcanism (Figure 3b).

6. Discussion: What Controls the Maximum Depth of Decoupling?

[63] The downdip termination of interface decoupling at a common depth requires a process in subduction zones that weakens the mantle rock or strengthens the interface at this depth. This process needs to be relatively insensitive to the temperature condition that varies significantly along the plate interface among different subduction zones.

[64] Although the dehydration of hydrous minerals is unlikely to control the MDD owing to the strong temperature dependence of dehydration reactions, changes in the strength of the hydrous minerals with depth may control the MDD. Although the strength of hydrous minerals depends also on temperature, what is important is how their strength changes with depth relative to the strength of the overriding mantle. Recent laboratory results show that during dislocation creep, antigorite is significantly weaker than wet olivine at shallow depths, but the decrease in their strength with depth due to increasing temperature is more prominent for wet olivine than for antigorite, resulting in a decrease in the strength contrast between them [*Hilairet et al.*, 2007]. The MDD may be regulated by the eventual disappearance of the strength contrast between the antigorite-bearing material along the interface and the less hydrated overriding mantle with increasing depth.

[65] The strength of the mantle is strongly temperature-dependent. Back-arc heat flows for most subduction zones are about 80 mW/m^2 and are likely to be governed by a common process of small-scale convection [*Currie and Hyndman*, 2006]. This probably determines the amount of heat supply into the arc and fore-arc region and thus regulates the overall strength of the fore-arc mantle uniformly among different subduction zones. The effects of the back-arc mantle thermal state on the fore-arc mantle thermal structure and rheology may give rise to an inherent scale length, which could regulate the MDD. Regardless of the specific mechanism, the common MDD is consistent with the fairly uniform back-arc heat flow among subduction zones and therefore appears to be an expression of the subduction zone heat budget [*Currie et al.*, 2004].

[66] It will be useful to develop dynamic models with a self-consistent mechanism that controls the MDD, and our modeling results should provide guidance for the future development of these models.

7. Conclusions

[67] A wide range of geophysical processes in subduction zones are known to depend on the thermal state of the subducting slab. Our compilation of geological and geophysical observations demonstrates systematic variations of subduction zone processes with the thermal parameter, φ, of the subducting slab: in subduction zones with colder slabs, a layer of relatively low seismic-wave speed in the top part of the subducting slab, representing the untransformed basaltic crust, and the intraslab seismicity extend to greater depths, and arc volcanism is more intense. ETS and mantle wedge serpentinization appear to be rare or less abundant in cold-slab subduction zones, possibly indicating their dependence on the slab thermal state. In contrast, the configuration of subduction zones is surprisingly uniform in that the slab beneath the arc is predominantly at 90–110 km depths regardless of the thermal state of the slab.

[68] Toward reconciling this uniformity and diversity of subduction zones, we hypothesize that the subducting slab and the overriding mantle are decoupled to a common depth of 70–80 km depth in most, if not all subduction zones, and the onset of mantle wedge flow downdip of the decoupled interface controls the uniform subduction zone configuration without significantly affecting the systematic variations in slab-age-dependent subduction zone processes. To test this hypothesis, we have developed thermal models for seventeen subduction zones by prescribing interface decoupling to 75 km depth. The models explain available surface heat flow observations.

[69] The thermal models predict that the region of high temperatures (>1200°C) and thus mantle melting occurs where the slab is at ~100 km depth and deeper for all seventeen subduction zones. In contrast, the mantle wedge in most of the fore arc is stagnant and cold, explaining why arc volcanism does not occur in the fore-arc region. Because of the sudden onset of mantle wedge flow at 70–80 km depth, crustal dehydration in most subduction zones peaks at depths shallower than 140 km.

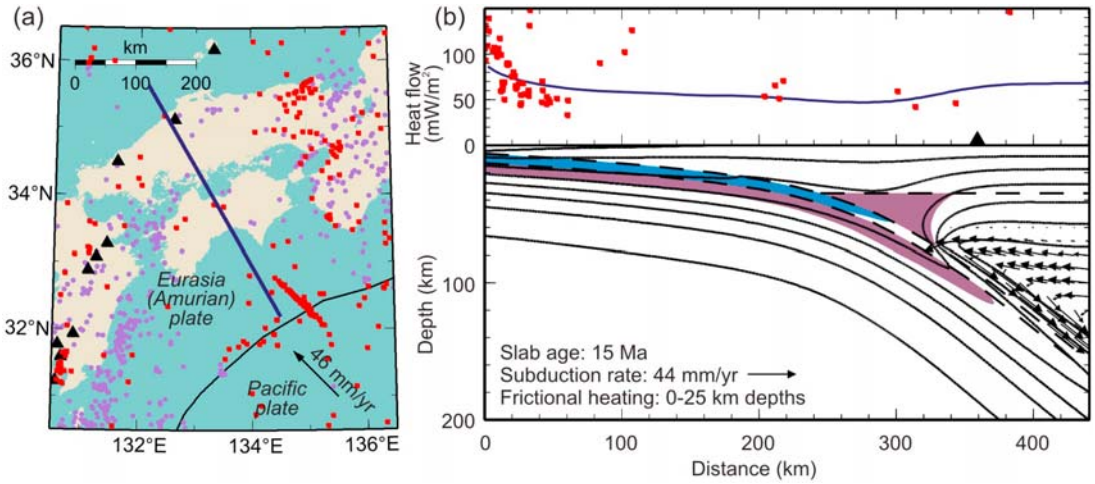

Figure A1. (a) Map and (b) modeling results for Nankai (index number 2). We adopted the slab geometry model reported by *Wang et al.* [2004] based primarily on the distribution of intraslab earthquakes. Their model, however, is only for the shallow part (<60 km depth) of the slab owing to lack of deeper intraslab earthquakes. Therefore, we extrapolated the deeper part of the slab from their model. Heat flow data are from *Tanaka et al.* [2004]. The observed surface heat flow near the trench is higher than predicted from the age of the plate and very sharply decreases landward. This has been explained to be the consequence of redistribution of heat by hydrothermal circulation in the relatively permeable subducting crust [*Spinelli and Wang*, 2008]. The regional-scale thermal model shown here does not address this effect.

The much reduced fluid supply from the subducting slab to the overriding mantle wedge downdip of this depth explains why arc volcanism does not tend to occur in the back arc even though the mantle is as hot as beneath the arc. Therefore, the common MDD controls the location of arc and can explain the uniform configuration of subduction zones. Even with a given MDD, the location of the arc can still be affected by other kinematic parameters and the path of ascending arc magma as a second-order effects.

[70] Our model predictions are also consistent with the observed systematic variations of subduction zone processes. The model-predicted depths of dehydration in both the subducting crust and mantle are deeper for colder slabs, consistent with the observed increase in the maximum depth of an LVL and intraslab seismicity with φ. The models also predict that fluid supply near the fore-arc mantle wedge tip is significantly smaller in cold-slab subduction zones because of deeper slab dehydration than in warm-slab subduction zones, possibly explaining why there is less evidence for mantle wedge serpentinization and ETS in cold-slab subduction zones. However, deeper slab dehydration in cold-slab subduction zones provides more fluid to the subarc mantle than in warm-slab subduction zones, consistent with the increasing intensity of arc volcanism with φ. The sudden onset of mantle wedge flow downdip of the decoupled interface also affects the slab thermal state but uniformly among different subduction zones owing to the common MDD, and therefore any systematic variations that depend on the slab thermal state are unaffected.

[71] In this study, we showed that a common depth of slab-mantle wedge decoupling reconciles the uniformity and diversity of subduction zones. Decoupling reflects a contrast between a stronger mantle wedge and a weaker subduction interface. The onset of coupling thus reflects the loss of the strength contrast. A mechanism that can reduce the strength contrast at a common depth of 70–80 km is the key to understanding the seemingly complex subduction zone geodynamics and is a critical subject of future research.

Appendix A: Modeling Results for Thirteen Subduction Zones

[72] In the main text, we discussed the modeling results obtained for seventeen subduction zones investigated in this study using two summary diagrams (Figures 8 and 9) and a summary (Table 5) but presented modeling results only for four subduction zones. Here, we present results for the remaining thirteen subduction zones. In all models,

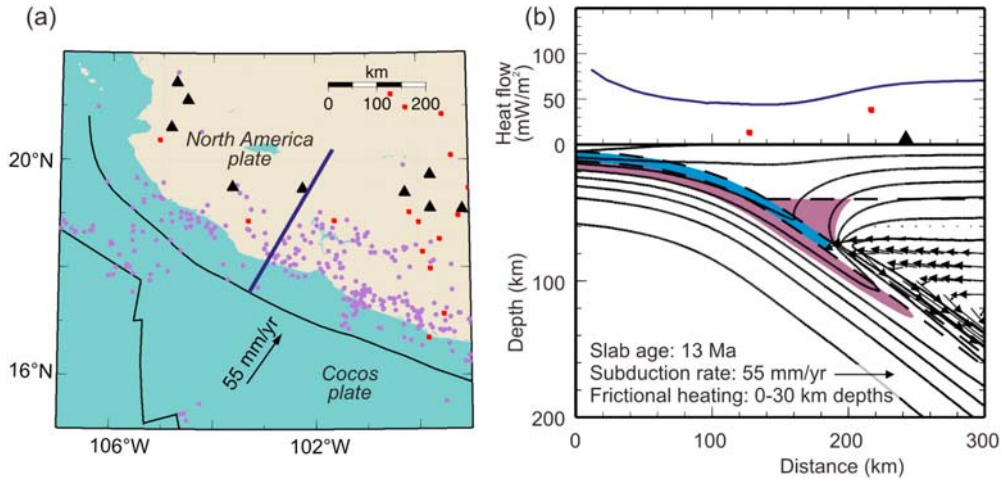

Figure A2. (a) Map and (b) modeling results for Mexico (index number 3). We adopted the slab geometry model of *Currie et al.* [2002], which was obtained using earthquake locations determined with the local seismic network. Heat flow data are from GHFD.

a common MDD of 75 km is assumed, and the boundary conditions and material properties are as described in the main text. How the slab geometry is obtained for each model is described in the figure captions. For all the thirteen subduction zones, surface heat flow measurements within 100 km of the profile line are plotted with the model-predicted surface heat flow values except for SC and northern Chile and Kermadec. For SC Chile, we include surface heat flow values derived from the depths of bottom simulating reflectors (BSR) that were imaged at ~120 km south of our profile line [*Grevemeyer et al.*, 2003], and we also include one measurement made at ~110 km north of the profile line (GHFD). For northern Chile and Kermadec, we include measurements within 200 km and 150 km, respectively, of the respective profile line (GHFD). References for the surface heat flow data for each margin are given in Table 2 and in the figure captions.

[73] Out of the thirteen subduction zones, ten are from continental margins, and the other three are from ocean-ocean margins. Results for continental

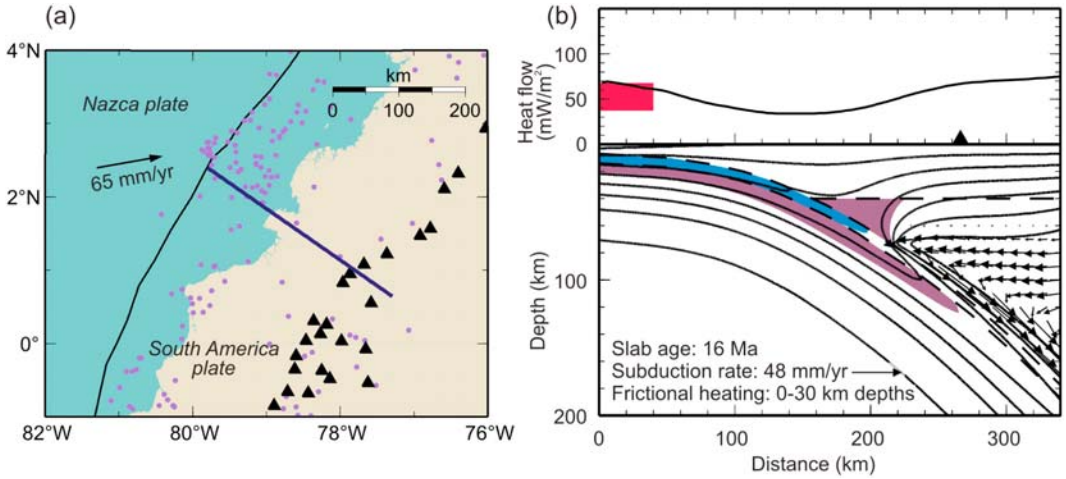

Figure A3. (a) Map and (b) modeling results for Colombia-Ecuador (index number 4). For the shallow part of the subducting slab, we adopted the slab geometry reported by *Marcaillou et al.* [2006, 2008] based on seismic reflection data. For the deeper part, we inferred the slab geometry from the distribution of earthquake hypocenters in the EHB catalog. The red rectangle in Figure A3b indicates the range of BSR-derived heat flow values (not shown on the map) measured within a 50-km distance from the profile line [*Marcaillou et al.*, 2006].

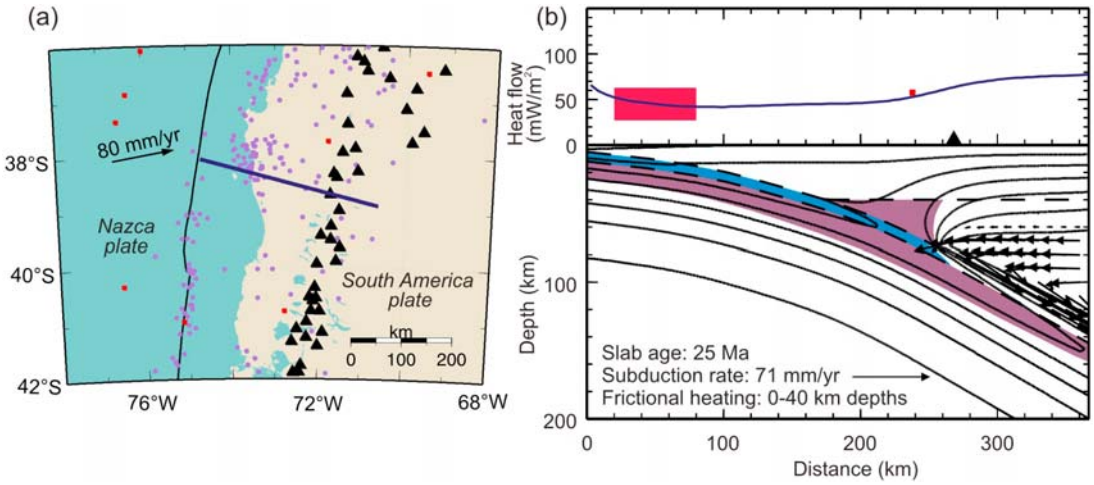

Figure A4. (a) Map and (b) modeling results for SC Chile (index number 5). We adopted the shallow part of the slab geometry that *Groß et al.* [2008] obtained from seismic reflection data and inferred the deeper part from earthquake hypocenters in the EHB catalog and the subarc slab depths determined by *Syracuse and Abers* [2006]. The red rectangle in Figure A4b indicates the range of BSR-derived heat flow values (not shown on the map) measured at ~120 km south of the profile line [*Grevemeyer et al.*, 2003]. The rest of the heat flow data (red dots) are from GHFD.

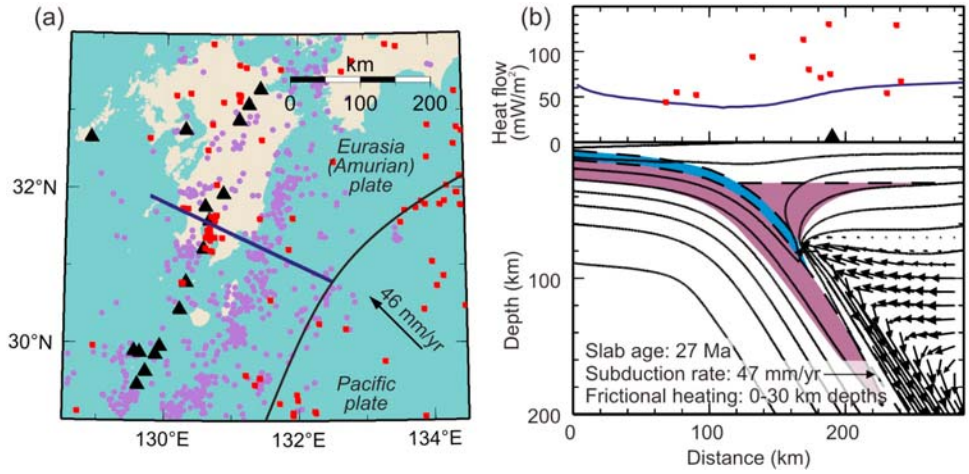

Figure A5. (a) Map and (b) modeling results for Kyushu (index number 6). We adopted the slab geometry model reported by *Wang et al.* [2004] based primarily on intraslab earthquake distribution. Heat flow data are from *Tanaka et al.* [2004].

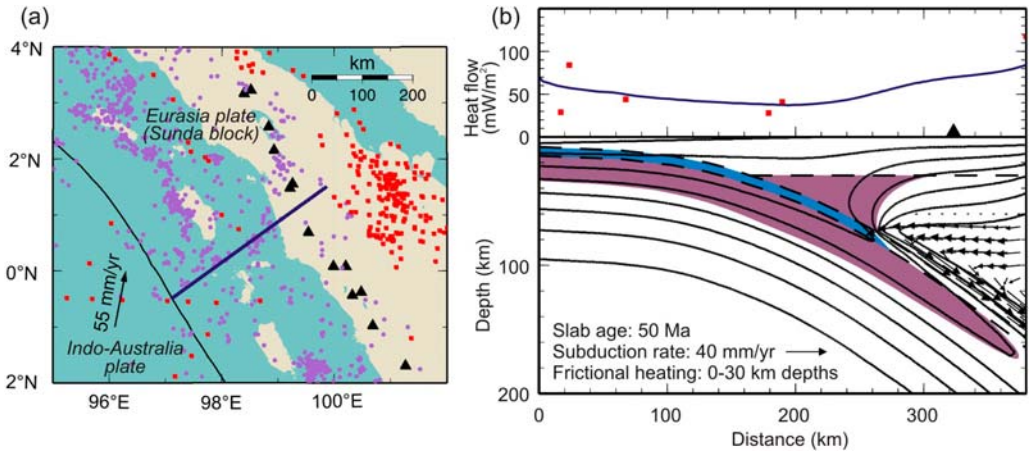

Figure A6. (a) Map and (b) modeling results for northern Sumatra (index number 7). We inferred the slab geometry from the distribution of earthquake hypocenters in the EHB catalog and the subarc slab depths determined by *England et al.* [2004]. Heat flow data are from GHFD.

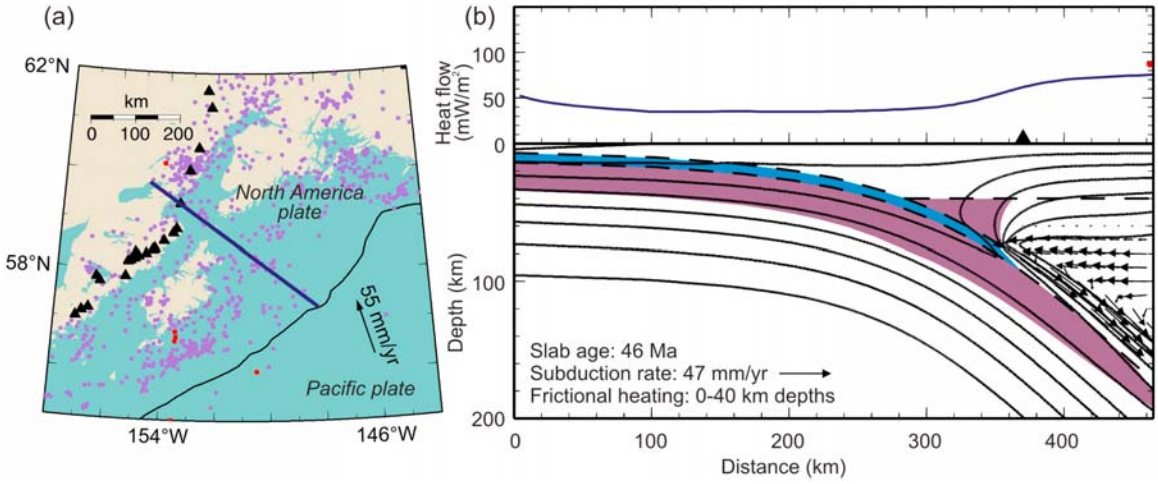

Figure A7. (a) Map and (b) modeling results for Alaska (index number 8). We adopted the slab geometry of *Oleskevich et al.* [1999], which was obtained by using seismic reflection and refraction data and earthquake distribution. Heat flow data are from GHFD.

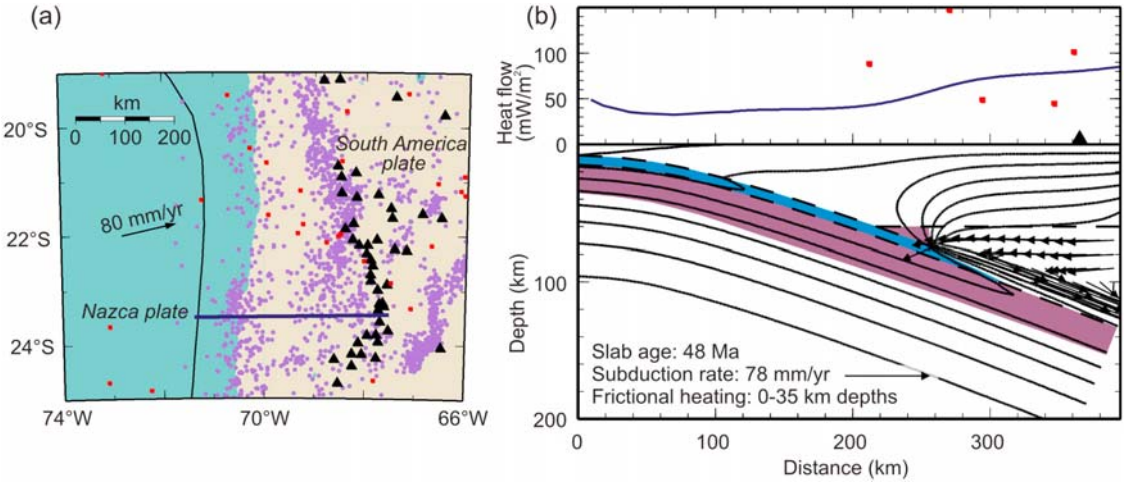

Figure A8. (a) Map and (b) modeling results for northern Chile (index number 9). For the shallow part, we adopted the slab geometry reported by *Sallarès and Ranero* [2005] and inferred the deeper part from earthquake hypocenters in the EBH catalog. However, the composite model indicates a relatively sharp bending at shallow depth (<30 km), which is mechanically less plausible for the relatively old slab. We thus reduced the sharpness of the slab curvature slightly in our model construction. Heat flow data are from GHFD.

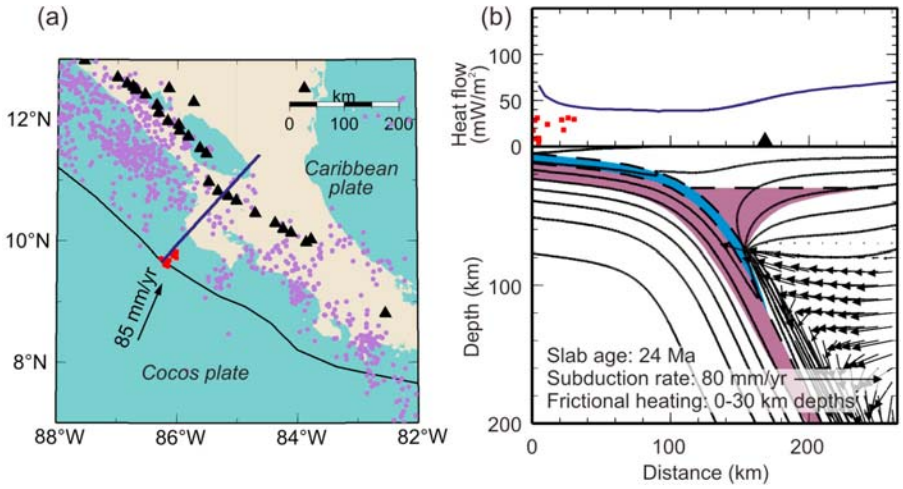

Figure A9. (a) Map and (b) modeling results for northern Costa Rica (index number 10). We adopted the slab geometry of *Peacock et al.* [2005], which was inferred from earthquake hypocenters in the EHB catalog and those determined by *Protti et al.* [1995] and *Newman et al.* [2002] using local networks. The slab geometry model is consistent with the subarc slab depth determined by *Syracuse and Abers* [2006]. Surface heat flow data are from *Langseth and Silver* [1996] and *Kimura et al.* [1997]. In northern Costa Rica, seismic images of the incoming Cocos plate, which was formed along the East Pacific Rise, show bending-related faults penetrating to 18–20 km depth, well into the oceanic mantle [*Ranero et al.*, 2003]. Common occurrence of basement outcrops on this plate segment, along with these deeply cutting faults, is thought to allow vigorous hydrothermal circulation and efficient extraction of heat from the basement [*Harris and Wang*, 2002; *Fisher et al.*, 2003]. Our regional-scale model does not include this effect. This explains the low observed heat flow values near the trench compared to the predicted values.

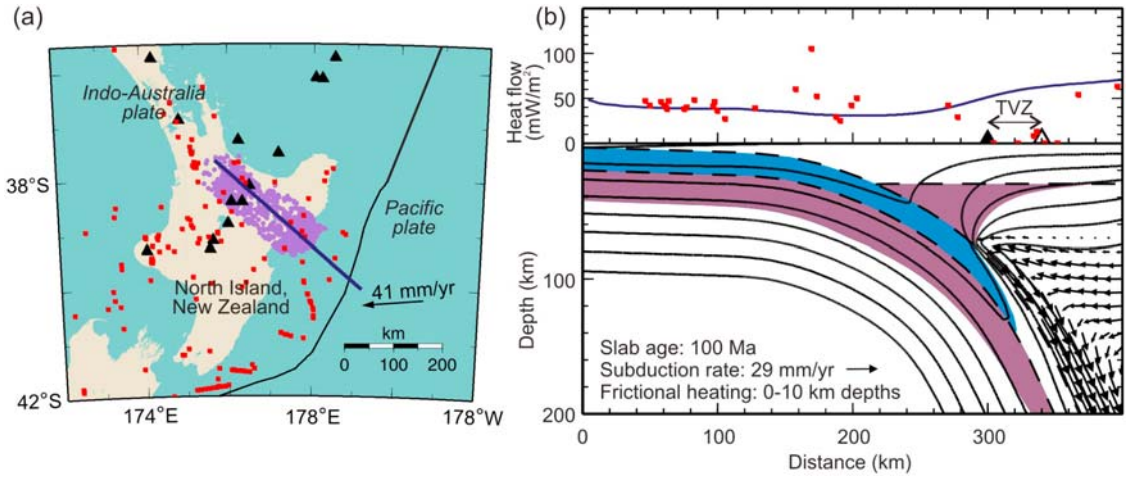

Figure A10. (a) Map and (b) modeling results for northern Hikurangi (index number 12). We use the slab geometry model of *Reyners et al.* [2006], which is delineated by the distribution of intraslab earthquakes (purple dots) located by the local network. Offshore heat flow data plotted in Figure A10b are from *Townend* [1997] and the rest plotted in Figure A10b are from GHFD. TVZ, Taupo Volcanic Zone. The open triangle represents the landward end of the ~40-km-wide TVZ.

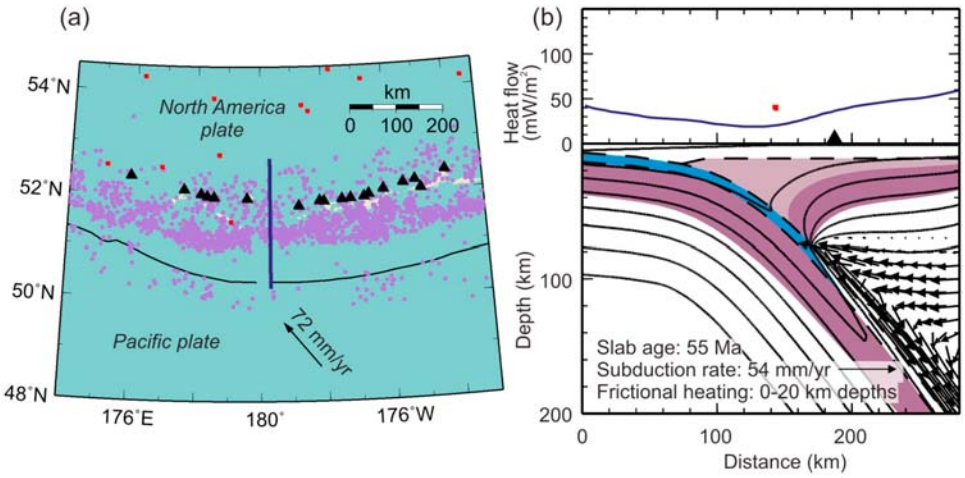

Figure A11. (a) Map and (b) modeling results for Aleutians (index number 11). We inferred the slab geometry from the distribution of intraslab earthquake hypocenters in the EHB catalog. In the model, the depth of the slab beneath the arc is 95 km, intermediate of two subarc slab depths obtained by *England et al.* [2004] for the regions east and west of our study region. Heat flow data are from GHFD.

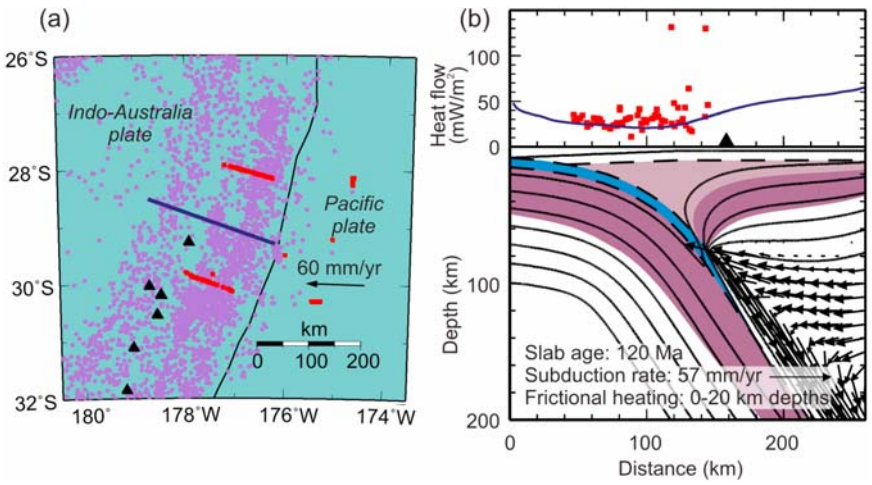

Figure A12. (a) Map and (b) modeling results for Kermadec (index number 14). We inferred the slab geometry from the distribution of intraslab earthquake hypocenters in the EHB catalog and the subarc slab depths determined by *England et al.* [2004]. Heat flow data are from *von Herzen et al.* [2001].

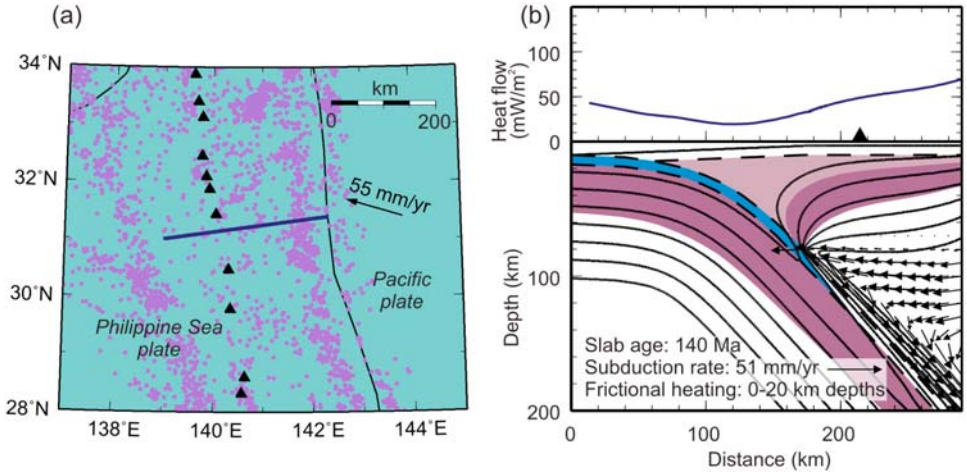

Figure A13. (a) Map and (b) modeling results for Izu (index number 16). We inferred the slab geometry from the distribution of intraslab earthquake hypocenters in the EHB catalog and the subarc slab depths determined by *England et al.* [2004]. Heat flow data are from GHFD.

margins are presented in Figures A1 through A10, and those for ocean-ocean margins are presented in Figures A11 through A13. As discussed in the main text, the models predict that the dominant serpentine species in a hydrated mantle wedge differs between the two types of margins. At continental margins, antigorite is the dominant species. At ocean-ocean margins, lower-temperature serpentine species chrysotile and lizardite are likely to be more abundant because the mantle wedge beneath the thin overriding oceanic crust is at shallow depths where fluid supply for serpentinization also includes the collapse of pore space in the subducting sediments and crust.

[74] The reader is referred to Figure 5 for the explanation of symbols.

Acknowledgments

[75] We thank J. He for developing the modeling code and for his assistance in the thermal modeling. We thank P. van Keken, G. Abers, R. Hyndman, S. Peacock, and M. Bostock for fruitful discussion. The paper benefited from reviews by Boris Kaus and Susanne Buiter. This research was partially supported by a Natural Sciences and Engineering Research Council of Canada Discovery grant to K. Wang. This is Geological Survey of Canada contribution 20090128.

References

Abers, G. A. (2005), Seismic low-velocity layer at the top of subducting slabs: Observations, predictions, and systematics, *Phys. Earth Planet. Inter.*, *149*, 7–29, doi:10.1016/j.pepi.2004.10.002.

Abers, G. A., P. E. van Keken, E. A. Kneller, A. Ferris, and J. C. Stachnik (2006), The thermal structure of subduction zones constrained by seismic imaging: Implications for slab dehydration and wedge flow, *Earth Planet. Sci. Lett.*, *241*, 387–397, doi:10.1016/j.epsl.2005.11.055.

Atwater, T. (1989), Plate tectonic history of the Northeast Pacific and western North America, in *The Eastern Pacific Ocean and Hawaii*, *Geol. of North Am.*, vol. N., edited by E. L. Winterer, D. M. Hussong, and R. W. Decker, pp. 21–72, Geol. Soc. of Am., Boulder, Colo.

Baba, T., Y. Tanioka, P. R. Cummins, and K. Uhira (2002), The slip distribution of the 1946 Nankai earthquake estimated from tsunami inversion using a new place model, *Phys. Earth Planet. Inter.*, *132*, 59–73, doi:10.1016/S0031-9201(02)00044-4.

Barckhausen, U., C. R. Ranero, R. von Huene, S. C. Cande, and H. A. Roeser (2001), Revised tectonic boundaries in the Cocos plate off Costa Rica: Implications for the segmentation of the convergent margin and for plate tectonic models, *J. Geophys. Res.*, *106*, 19,207–19,220, doi:10.1029/2001JB000238.

Blakely, R. J., T. M. Brocher, and R. E. Wells (2005), Subduction-zone magnetic anomalies and implications for hydrated forearc mantle, *Geology*, *33*, 445–448, doi:10.1130/G21447.1.

Bock, G., B. Schurr, and G. Asch (2000), High-resolution image of the oceanic Moho in the subducting Nazca plate from P–S converted waves, *Geophys. Res. Lett.*, *27*, 3929–3932, doi:10.1029/2000GL011881.

Bock, Y., L. Prawirodirdjo, J. F. Genrich, C. Stevens, R. McCaffrey, C. Subarya, S. S. O. Puntodewo, and E. Calais (2003), Crustal motion in Indonesia from GPS measurements, *J. Geophys. Res.*, *108*(B8), 2367, doi:10.1029/2001JB000324.

Bostock, M. G., R. D. Hyndman, S. Rondenay, and S. M. Peacock (2002), An inverted continental Moho and serpentinization of the forearc mantle, *Nature*, *417*, 536–538, doi:10.1038/417536a.

Brocher, T. M., R. Parsons, A. M. Trehu, S. M. Snelson, and M. A. Fisher (2003), Seismic evidence for widespread serpentinized forearc upper mantle along the Cascadia margin, *Geology*, *31*, 267–270, doi:10.1130/0091-7613(2003)031<0267:SEFWSF>2.0.CO;2.

Brudzinski, M. R., C. H. Thurber, B. R. Hacker, and E. R. Engdahl (2007), Global prevalence of double Benioff zones, *Science*, *316*, 1472–1474, doi:10.1126/science.1139204.

Cagnioncle, A.-M., E. M. Parmentier, and L. T. Elkins-Tanton (2007), Effect of solid flow above a subducting slab on water distribution and melting at convergent plate boundaries, *J. Geophys. Res.*, *112*, B09402, doi:10.1029/2007JB004934.

Cande, S. C., and D. V. Kent (1995), Revised calibration of the geomagnetic polarity timescale for the late Cretaceous and Cenozoic, *J. Geophys. Res.*, *100*, 6093–6095, doi:10.1029/94JB03098.

Carlson, R. L., and D. J. Miller (2003), Mantle wedge water contents estimated from seismic velocities in partially serpentinized peridotites, *Geophys. Res. Lett.*, *30*(5), 1250, doi:10.1029/2002GL016600.

Carlson, R. L., D. J. Miller, and J. Newman (2009), Olivine enigma: Why alteration controls the seismic properties of oceanic gabbros, *Geochem. Geophys. Geosyst.*, *10*, Q03O16, doi:10.1029/2008GC002263.

Cassidy, J. F., and R. M. Ellis (1993), S-wave velocity structure of the northern Cascadia subduction zone, *J. Geophys. Res.*, *98*, 4407–4421, doi:10.1029/92JB02696.

Cassidy, J. F., and F. Waldhauser (2003), Evidence for both crustal and mantle earthquakes in the subducting Juan de Fuca plate, *Geophys. Res. Lett.*, *30*(2), 1095, doi:10.1029/2002GL015511.

Christensen, N. I. (2004), Serpentinites, peridotites, and seismology, *Int. Geol. Rev.*, *46*, 795–816, doi:10.2747/0020-6814.46.9.795.

Clift, P., and P. Vannucchi (2004), Controls on tectonic accretion versus erosion in subduction zones: Implications for the origin and recycling of the continental crust, *Rev. Geophys.*, *42*, RG2001, doi:10.1029/2003RG000127.

Crisp, J. A. (1984), Rates of magma emplacement and volcanic output, *J. Volcanol. Geotherm. Res.*, *20*, 177–211, doi:10.1016/0377-0273(84)90039-8.

Currie, C. A., and R. D. Hyndman (2006), The thermal structure of subduction zone back arcs, *J. Geophys. Res.*, *111*, B08404, doi:10.1029/2005JB004024.

Currie, C. A., R. D. Hyndman, K. Wang, and V. Kostoglodov (2002), Thermal models of the Mexico subduction zone: Implications for the megathrust seismogenic zone, *J. Geophys. Res.*, *107*(B12), 2370, doi:10.1029/2001JB000886.

Currie, C. A., K. Wang, R. D. Hyndman, and J. He (2004), The thermal effects of steady-state slab-driven mantle flow above a subducting plate: The Cascadia subduction zone and back arc, *Earth Planet. Sci. Lett.*, *223*, 35–48, doi:10.1016/j.epsl.2004.04.020.

Davis, E. E., and R. D. Hyndman (1989), Accretion and recent deformation of sediments along the northern Cascadia subduction zone, *Geol. Soc. Am. Bull.*, *101*, 1465–1480, doi:10.1130/0016-7606(1989)101<1465:AARDOS>2.3.CO;2.

Davy, B., and R. A. Wood (1994), Gravity and magnetic modelling of the Hikurangi Plateau, *Mar. Geol.*, *118*, 139–151, doi:10.1016/0025-3227(94)90117-1.

Defant, M. J., and M. S. Drummond (1993), Mount St. Helens: Potential example of the partial melting of the subducted lithosphere in a volcanic arc, *Geology*, *21*, 547–550, doi:10.1130/0091-7613(1993)021<0547:MSHPEO>2.3.CO;2.

DeMets, C., R. G. Gordon, D. F. Argus, and S. Stein (1990), Current plate motions, *Geophys. J. Int.*, *101*, 425–478, doi:10.1111/j.1365-246X.1990.tb06579.x.

DeMets, C., R. G. Gordon, D. F. Argus, and S. Stein (1994), Effect of recent revisions to the geomagnetic time-scale on estimate of current plate motions, *Geophys. Res. Lett.*, *21*, 2191–2194, doi:10.1029/94GL02118.

DeMets, D. C. (2001), A new estimate for present-day Cocos-Caribbean plate motion: Implications for slip along the Central American volcanic arc, *Geophys. Res. Lett.*, *28*, 4043–4046, doi:10.1029/2001GL013518.

DeShon, H. R., and S. Y. Schwartz (2004), Evidence for serpentinization of the forearc mantle wedge along the Nicoya Peninsula, Costa Rica, *Geophys. Res. Lett.*, *31*, L21611, doi:10.1029/2004GL021179.

Dimalanta, C., A. Taira, G. P. Yumul Jr., H. Tokuyama, and K. Mochizuki (2002), New rates of western Pacific island arc magmatism from seismic and gravity data, *Earth Planet. Sci. Lett.*, *202*, 105–115, doi:10.1016/S0012-821X(02)00761-6.

Eberhart-Phillips, D., M. Reyners, M. Chadwick, and G. Stuart (2008), Three-dimensional attenuation structure of the Hikurangi subduction zone in the central North Island, New Zealand, *Geophys. J. Int.*, *174*, 418–434, doi:10.1111/j.1365-246X.2008.03816.x.

Engdahl, E. R., R. D. Van der Hilst, and R. P. Buland (1998), Global teleseismic earthquake relocation with improved travel times and procedures for depth determination, *Bull. Seismol. Soc. Am.*, *88*, 722–743.

England, P., R. Engdahl, and W. Thatcher (2004), Systematic variation in the depths of slabs beneath arc volcanoes, *Geophys. J. Int.*, *156*, 377–408, doi:10.1111/j.1365-246X.2003.02132.x.

Evans, B. W. (1977), Metamorphism of alpine peridotite and serpentinite, *Annu. Rev. Earth Planet. Sci.*, *5*, 397–447, doi:10.1146/annurev.ea.05.050177.002145.

Evans, B. W. (2004), The serpentine multisystem revised: Chrysotile is metastable, *Int. Geol. Rev.*, *46*, 479–506, doi:10.2747/0020-6814.46.6.479.

Fisher, A. T., C. A. Stein, R. N. Harris, K. Wang, E. A. Silver, M. Pfender, M. Hutnak, A. Cherkaoui, R. Bodzin, and H. Villinger (2003), Abrupt thermal transition reveals hydrothermal boundary and role of seamounts within the Cocos Plate, *Geophys. Res. Lett.*, *30*(11), 1550, doi:10.1029/2002GL016766.

Fryer, P. (1996), Evolution of the Mariana convergent plate margin system, *Rev. Geophys.*, *34*, 89–125, doi:10.1029/95RG03476.

Fukao, Y., S. Hori, and M. Ukawa (1983), A seismological constraint on the depth of basalt-eclogite transition in a subducting oceanic crust, *Nature*, *303*, 413–415, doi:10.1038/303413a0.

Furukawa, Y. (1993), Depth of the decoupling plate interface and thermal structure under arcs, *J. Geophys. Res.*, *98*, 20,005–20,013, doi:10.1029/93JB02020.

Gaetani, G. A., and T. L. Grove (1998), The influence of water on melting of mantle peridotite, *Contrib. Mineral. Petrol.*, *131*, 323–346, doi:10.1007/s004100050396.

Graeber, F. M., and G. Asch (1999), Three-dimensional models of *P* wave velocity and *P*-to-*S* ratio in the southern central Andes by simultaneous inversion of local earthquake data, *J. Geophys. Res.*, *104*, 20,237–20,256, doi:10.1029/1999JB900037.

Grevemeyer, I., J. L. Diaz-Naveas, C. R. Ranero, H. W. Villinger, and the ODP Leg 202 Scientific Party (2003), Heat flow over the descending Nazca plate in central Chile, 32°S to 41°S: Observations from ODP Leg 202 and the occurrence of natural gas hydrates, *Earth Planet. Sci. Lett.*, *213*, 285–298, doi:10.1016/S0012-821X(03)00303-0.

Groß, K., U. Micksch, and the TIPTEQ Research Group, Seismics Team (2008), The reflection seismic survey of project TIPTEQ–the inventory of the Chilean subduction zone at 38.2°S, *Geophys. J. Int.*, *172*, 565–571, doi:10.1111/j.1365-246X.2007.03680.x.

Grove, T. L., N. Chatterjee, S. W. Parman, and E. Medard (2006), The influence of H_2O on mantle wedge melting, *Earth Planet. Sci. Lett.*, *249*, 74–89, doi:10.1016/j.epsl.2006.06.043.

Grove, T. L., C. B. Till, E. Lev, N. Chatterjee, and E. Médard (2009), Kinematic variables and water transport control the formation and location of arc volcanoes, *Nature*, *459*, 694–697, doi:10.1038/nature08044.

Haberland, C., A. Rietbrock, D. Lange, K. Batalille, and S. Hofmann (2006), Interaction between forearc and oceanic plate at the south-central Chilean margin as seen in local seismic data, *Geophys. Res. Lett.*, *33*, L23302, doi:10.1029/2006GL028189.

Hacker, B. R., S. M. Peacock, G. A. Abers, and S. D. Holloway (2003), Subduction factory: 2. Are intermediate-depth earthquakes in subducting slabs linked to metamorphic dehydration?, *J. Geophys. Res.*, *108*(B1), 2030, doi:10.1029/2001JB001129.

Hardy, N. C. (1991), Tectonic evolution of the easternmost Panama Basin: Some new data and interferences, *J. South Am. Earth Sci.*, *4*, 261–269, doi:10.1016/0895-9811(91)90035-J.

Harris, R. N., and K. Wang (2002), Thermal models of the Middle America Trench at the Nicoya Peninsula, Costa Rica, *Geophys. Res. Lett.*, *29*(21), 2010, doi:10.1029/2002GL015406.

Hasegawa, A., S. Horiuchi, and N. Umino (1994), Seismic structure of the northeastern Japan convergent margin: A synthesis, *J. Geophys. Res.*, *99*, 22,295–22,311, doi:10.1029/93JB02797.

Hilairet, N., B. Reynard, Y. Wang, I. Daniel, S. Merkel, N. Nishiyama, and S. Petitgirard (2007), High-pressure creep of serpentine, interseismic deformation, and initiation of subduction, *Science*, *318*, 1910–1913, doi:10.1126/science.1148494.

Hippchen, S., and R. D. Hyndman (2008), Thermal and structural models of the Sumatra subduction zone: Implications for the megathrust seismogenic zone, *J. Geophys. Res.*, *113*, B12103, doi:10.1029/2008JB005698.

Hochstein, M. P. (1995), Crustal heat transfer in the Taupo Volcanic Zone (New Zealand): Comparison with other volcanic arcs and explanatory heat source models, *J. Volcanol. Geotherm. Res.*, *68*, 117–151, doi:10.1016/0377-0273(95)00010-R.

Hori, S. (1990), Seismic waves guided by untransformed oceanic crust subducting into the mantle: The case of the Kanto district, *Tectonophysics*, *176*, 355–376, doi:10.1016/0040-1951(90)90078-M.

Hori, S., H. Inoue, Y. Fukao, and M. Ukawa (1985), Seismic detection of the untransformed 'basaltic' oceanic crust subducting into the mantle, *Geophys. J. R. Astron. Soc.*, *83*, 169–197.

Hyndman, R. D., and S. M. Peacock (2003), Serpentinization of the forearc mantle, *Earth Planet. Sci. Lett.*, *212*, 417–432, doi:10.1016/S0012-821X(03)00263-2.

Ito, E., and T. Katsura (1989), A temperature profile of the mantle transition zone, *Geophys. Res. Lett.*, *16*, 425–428, doi:10.1029/GL016i005p00425.

Kamimura, A., J. Kasahara, R. Hino, M. Shinohara, R. Hino, H. Shiobara, G. Fujie, and T. Kanazawa (2002), Crustal structure study at the Izu-Bonin subduction zone around 31°N: Implications of serpentinized materials along the subduction plate boundary, *Phys. Earth Planet. Inter.*, *132*, 105–129, doi:10.1016/S0031-9201(02)00047-X.

Kamiya, S., and Y. Kobayashi (2000), Seismological evidence for existence of serpentinized wedge mantle, *Geophys. Res. Lett.*, *27*, 819–822, doi:10.1029/1999GL011080.

Kao, H., S. J. Shan, H. Dragert, G. Rogers, J. F. Cassidy, and K. Ramachandran (2005), Depth distribution of seismic tremors along the northern Cascadia margin, *Nature*, *436*, 841–844, doi:10.1038/nature03903.

Karato, S., and P. Wu (1993), Rheology of the upper mantle: A synthesis, *Science*, *260*, 771–778, doi:10.1126/science.260.5109.771.

Kawakatsu, H., and S. Watada (2007), Seismic evidence for deep-water transportation in the mantle, *Science*, *316*, 1468–1471, doi:10.1126/science.1140855.

Kelemen, P. B., J. Rilling, E. M. Parmentier, L. Mehl, and B. R. Hacker (2003), Thermal structure due to solid-state flow in the mantle wedge beneath arcs, in *Inside the Subduction Factory*, *Geophys. Monogr. Ser*, vol. 138, edited by J. Eiler, pp. 293–311, AGU, Washington, D. C.

Kimura, G., E. A. Silver, and P. Blum (1997), *Proceedings of the Ocean Drilling Program, Initial Reports*, vol. 170, Ocean Drill. Program, College Station, Tex.

Kirby, S. H., E. R. Engdahl, and R. Denlinger (1996), Intermediate-depth intraslab earthquakes and arc volcanism as physical expressions of crustal and uppermost mantle metamorphism in subducting slabs, in *Subduction: Top to Bottom*, *Geophys. Monogr. Ser*, vol. 96, edited by G. E. Bebout et al., pp. 195–214, AGU, Washington, D. C.

Kneller, E. A., P. E. van Keken, S. Karato, and J. Park (2005), B-type olivine fabric in the mantle wedge: Insights from high-resolution non-Newtonian subduction zone models, *Earth Planet. Sci. Lett.*, *237*, 781–797, doi:10.1016/j.epsl.2005.06.049.

Kodaira, S., T. Sato, N. Takahashi, A. Ito, Y. Tamura, Y. Tatsumi, and Y. Kaneda (2007), Seismological evidence for variable growth of crust along the Izu intraoceanic arc, *J. Geophys. Res.*, *112*, B05104, doi:10.1029/2006JB004593.

Kohut, E. J., R. J. Stern, A. J. R. Kent, R. L. Nielsen, S. J. Bloomer, and M. Leybourne (2006), Evidence for adiabatic decompression melting in the Southern Mariana Arc from high-Mg lavas and melt inclusions, *Contrib. Mineral. Petrol.*, *152*, 201–221, doi:10.1007/s00410-006-0102-7.

Kostoglodov, V., and W. Bandy (1995), Seismotectonic constraints on the convergence rate between the Rivera and North American plates, *J. Geophys. Res.*, *100*, 17,977–17,989, doi:10.1029/95JB01484.

Koulakov, I., S. V. Sobolev, and G. Asch (2006), P- and S-velocity images of the lithosphere-asthenosphere system in the central Andes from local-source tomographic inversion, *Geophys. J. Int.*, *167*, 106–126, doi:10.1111/j.1365-246X.2006.02949.x.

Langseth, M. G., and E. A. Silver (1996), The Nicoya convergent margin—A region of exceptionally low heat flow, *Geophys. Res. Lett.*, *23*, 891–894, doi:10.1029/96GL00733.

Larson, K. M., V. Kostoglodov, S. Miyazaki, and J. A. Santiago (2007), The 2006 aseismic slow slip event in Guerrero, Mexico: New results from GPS, *Geophys. Res. Lett.*, *34*, L13309, doi:10.1029/2007GL029912.

Lee, C., and S. D. King (2009), Effect of mantle compressibility on the thermal and flow structures of the subduction zones, *Geochem. Geophys. Geosyst.*, *10*, Q01006, doi:10.1029/2008GC002151.

Lewis, T. J., W. H. Bentkowski, E. E. Davis, R. D. Hyndman, J. G. Souther, and J. A. Wright (1988), Subduction of the Juan de Fuca Plate: Thermal consequences, *J. Geophys. Res.*, *93*, 15,207–15,225, doi:10.1029/JB093iB12p15207.

Magee, M. E., and M. D. Zoback (1993), Evidence for a weak interpolate thrust fault along the northern Japan subduction zone and implications for the mechanics of thrust faulting and fluid expulsion, *Geology*, *21*, 809–812, doi:10.1130/0091-7613(1993)021<0809:EFAWIT>2.3.CO;2.

Marcaillou, B., G. Spence, J.-Y. Collot, and K. Wang (2006), Thermal regime from bottom simulating reflectors along the north Ecuador–south Colombia margin: Relation to margin segmentation and great subduction earthquakes, *J. Geophys. Res.*, *111*, B12407, doi:10.1029/2005JB004239.

Marcaillou, B., G. Spence, K. Wang, J.-Y. Collot, and A. Ridodetti (2008), Thermal segmentation along the N. Ecuador-S. Colombia margin (1–4°N): Prominent influence of sedimentation rate in the trench, *Earth Planet. Sci. Lett.*, *272*, 296–308, doi:10.1016/j.epsl.2008.04.049.

Matsuzawa, T., N. Umino, A. Hasegawa, and A. Takagi (1986), Upper mantle velocity structure estimated from PS-converted wave beneath the north-eastern Japan Arc, *Geophys. J. R. Astron. Soc.*, *86*, 767–787.

McCrory, P. A., J. L. Blair, D. H. Oppenheimer, and S. R. Walter (2004), Depth to the Juan de Fuca slab beneath the Cascadia subduction margin: A 3-D model for sorting earthquakes [CD-ROM], *U.S. Geol. Surv. Data Ser., DS-91*.

McKenzie, D. (1969), Speculations on the consequences and causes of plate motion, *Geophys. J. R. Astron. Soc.*, *18*, 1–32.

Miura, S., N. Takahashi, A. Nakanishi, T. Tsuru, S. Kodaira, and Y. Kaneda (2005), Structural characteristics off Miyagi forearc region, the Japan Trench seismogenic zone, deduced from a wide-angle reflection and refraction study, *Tectonophysics*, *407*, 165–188, doi:10.1016/j.tecto.2005.08.001.

Molnar, P., D. Freedman, and J. Shih (1979), Lengths of intermediate and deep seismic zones and temperatures in downgoing slabs of lithosphere, *Geophys. J. R. Astron. Soc.*, *56*, 41–54.

Müller, R. D., W. R. Roest, J.-Y. Royer, L. M. Gahagan, and J. G. Sclater (1997), Digital isochrons of the world's ocean floor, *J. Geophys. Res.*, *102*, 3211–3214, doi:10.1029/96JB01781.

Nakajima, J., T. Matsuzawa, A. Hasegawa, and D. Zhao (2001), Three-dimensional structure of Vp, Vs, and Vp/Vs beneath northeastern Japan: Implications for arc magmatism and fluids, *J. Geophys. Res.*, *106*(B10), 21,843–21,858, doi:10.1029/2000JB000008.

Nakamura, M., H. Watanabe, T. Konomi, S. Kimura, and K. Moira (1997), Characteristic activities of subcrustal earthquakes along the outer zone of southwestern Japan (in Japanese), *Annu. Dis. Prev. Res. Inst. Kyoto Univ.*, *40*, B-1.

Newman, A. V., S. Y. Schwartz, V. Gonzalez, H. R. DeShon, and J. M. Protti (2002), Along-strike variability in the seismogenic zone below Nicoya Peninsula, Costa Rica, *Geophys. Res. Lett.*, *29*(20), 1977, doi:10.1029/2002GL015409.

Obara, K. (2002), Nonvolcanic deep tremor associated with subduction in southwest Japan, *Science*, *296*, 1679–1681, doi:10.1126/science.1070378.

Ohkura, T. (2000), Structure of the upper part of the Philippine Sea plate estimated by later phases of upper mantle earthquakes in and around Shikoku, Japan, *Tectonophysics*, *321*, 17–36, doi:10.1016/S0040-1951(00)00078-0.

Okino, K., Y. Shimakawa, and S. Nagaoka (1994), Evolution of the Shikoku Basin, *J. Geomagn. Geoelectr.*, *446*, 463–479.

Oleskevich, D. A., R. D. Hyndman, and K. Wang (1999), The updip and downdip limits to great subduction earthquakes: Thermal and structural models of Cascadia, south Alaska, SW Japan, and Chile, *J. Geophys. Res.*, *104*, 14,965–14,991, doi:10.1029/1999JB900060.

Pawley, A. R., and J. R. Holloway (1993), Water sources for subduction zone volcanism: New experimental constraints, *Science*, *260*, 664–667, doi:10.1126/science.260.5108.664.

Payero, J. S., V. Kostoglodov, N. Shapiro, T. Mikumo, A. Iglesias, X. Pérez-Campos, and R. W. Clayton (2008), Nonvolcanic tremor observed in the Mexican subduction zone, *Geophys. Res. Lett.*, *35*, L07305, doi:10.1029/2007GL032877.

Peacock, S. M. (2001), Are the lower planes of double seismic zones caused by serpentine dehydration in subducting oceanic mantle?, *Geology*, *29*, 299–302, doi:10.1130/0091-7613(2001)029<0299:ATLPOD>2.0.CO;2.

Peacock, S. M., and K. Wang (1999), Seismic consequences of warm versus cool subduction metamorphism: Examples from southwest and northeast Japan, *Science*, *286*, 937–939, doi:10.1126/science.286.5441.937.

Peacock, S. M., P. E. van Keken, S. D. Holloway, B. R. Hacker, G. A. Abers, and R. L. Fergason (2005), Thermal structure of the Costa Rica–Nicaragua subduction zone, *Phys. Earth Planet. Inter.*, *149*, 187–200, doi:10.1016/j.pepi.2004.08.030.

Pollack, H. N., S. J. Hurter, and J. R. Johnson (1993), Heat flow from the Earth's interior: Analysis of the global data set, *Rev. Geophys.*, *31*, 267–280, doi:10.1029/93RG01249.

Protti, M., F. Guendel, and K. McNally (1995), Correlation between the age of the subducting Cocos plate and the geometry of the Wadati-Benioff zone under Nicaragua and Costa Rica, in *Geologic and Tectonic Development of the Caribbean Plate Boundary in Southern Central America*, edited by P. Mann, *Spec. Pap. Geol. Soc. Am.*, *295*, 309–326.

Ramachandran, K., S. E. Doss, G. D. Spence, R. D. Hyndman, and T. M. Brocher (2005), Forearc structure beneath southwestern British Columbia: A three-dimensional tomographic velocity model, *J. Geophys. Res.*, *110*, B02303, doi:10.1029/2004JB003258.

Ranero, C. R., J. P. Morgan, K. McIntosh, and C. Reichert (2003), Bending-related faulting and mantle serpentinization at the Middle America trench, *Nature*, *425*, 367–373, doi:10.1038/nature01961.

Reyners, M., D. Eberhart-Phillips, G. Stuart, and Y. Nishimura (2006), Imaging subduction from the trench to 300 km depth beneath the central North Island, New Zealand, with Vp and Vp/Vs, *Geophys. J. Int.*, *165*, 565–583, doi:10.1111/j.1365-246X.2006.02897.x.

Reyners, M., D. Eberhart-Phillips, and G. Stuart (2007), The role of fluids in lower-crustal earthquakes near continental rifts, *Nature*, *446*, 1075–1078, doi:10.1038/nature05743.

Rondenay, S., G. A. Abers, and P. E. van Keken (2008), Seismic imaging of subduction zone metamorphism, *Geology*, *36*, 275–278, doi:10.1130/G24112A.1.

Sallarès, V., and C. R. Ranero (2005), Structure and tectonics of the erosional convergent margin off Antofagasta, north Chile (23°30′S), *J. Geophys. Res.*, *110*, B06101, doi:10.1029/2004JB003418.

Saltus, R. W., T. L. Hudson, and G. G. Connard (1999), A new magnetic view of Alaska, *GSA Today*, *9*, 2–6.

Schmidt, M. W., and S. Poli (1998), Experimentally based water budgets for dehydrating slabs and consequences for arc magma generation, *Earth Planet. Sci. Lett.*, *163*, 361–379, doi:10.1016/S0012-821X(98)00142-3.

Seno, T., and Y. Yamanaka (1996), Double seismic zones, compressional deep trench-outer rise events, and superplumes, in *Subduction: Top to Bottom*, *Geophys. Monogr. Ser*, vol. 96, edited by G. E. Bebout et al., pp. 347–355, AGU, Washington, D. C.

Seno, T., D. Zhao, Y. Kobayashi, and M. Nakamura (2001), Dehydration of serpentinized mantle: Seismic evidence from southwest Japan, *Earth Planets Space*, *53*, 861–871.

Shelly, D. R., G. C. Beroza, S. Ide, and S. Nakamula (2006), Low-frequency earthquakes in Shikoku, Japan, and their relationship to episodic tremor and slip, *Nature*, *442*, 188–191, doi:10.1038/nature04931.

Shelly, D. R., G. C. Beroza, and S. Ide (2007), Non-volcanic tremor and low-frequency earthquake swarms, *Nature*, *446*, 305–307, doi:10.1038/nature05666.

Shiomi, K., H. Sata, K. Obara, and M. Ohtake (2004), Configuration of subducting Philippine Sea plate beneath southwest Japan revealed from receiver function analysis based on the multivariate autoregressive model, *J. Geophys. Res.*, *109*, B04308, doi:10.1029/2003JB002774.

Spinelli, G. A., and K. Wang (2008), Effects of fluid circulation in subducting crust on Nankai margin seismogenic zone temperatures, *Geology*, *36*, 887–890, doi:10.1130/G25145A.1.

Stein, C. A., and S. Stein (1992), A model for the global variation in oceanic depth and heat flow with lithospheric age, *Nature*, *359*, 123–129, doi:10.1038/359123a0.

Syracuse, E. M., and G. A. Abers (2006), Global compilation of variations in slab depth beneath arc volcanoes and implications, *Geochem. Geophys. Geosyst.*, *7*, Q05017, doi:10.1029/2005GC001045.

Taira, A., et al. (1998), Nature and growth rate of the northern Izu-Bonin (Ogasawara) arc crust and their implications for continental crust formation, *Island Arc*, *7*, 395–407, doi:10.1111/j.1440-1738.1998.00198.x.

Takahashi, N., S. Kodaira, S. L. Klemperer, Y. Tatsumi, Y. Kaneda, and K. Suyehiro (2007), Crustal structure and evolution of the Mariana intra-oceanic island arc, *Geology*, *35*, 203–206, doi:10.1130/G23212A.1.

Tanaka, A., M. Yamano, Y. Yano, and M. Sasada (2004), Geothermal gradient and heat flow data in and around Japan, *Digital Geosci. Map DGMP-5*, Geol. Surv. of Jpn., Higashi, Japan.

Tatsumi, Y. (1986), Formation of the volcanic front in subduction zones, *Geophys. Res. Lett.*, *13*, 717–720, doi:10.1029/GL013i008p00717.

Tatsumi, Y., and S. Eggins (1995), *Subduction Zone Magmatism*, 211 pp., Blackwell Sci., Boston, Mass.

Tebbens, S. F., W. C. Cande, L. Kovacs, J. D. Parra, J. L. LaBrecque, and H. Vergara (1997), The Chile ridge: A tectonic framework, *J. Geophys. Res.*, *102*, 12,035–12,059, doi:10.1029/96JB02581.

Townend, J. (1997), Estimates of conductive heat flow through bottom-simulating reflectors on the Hikurangi and southwest Fiordland continental margins, New Zealand, *Mar. Geol.*, *141*, 209–220, doi:10.1016/S0025-3227(97)00073-X.

Ulmer, P. (2001), Partial melting in the mantle wedge—The role of H_2O in the genesis of mantle-derived "arc-related"

magmas, *Phys. Earth Planet. Inter.*, *127*, 215–232, doi:10.1016/S0031-9201(01)00229-1.

Ulmer, P., and V. Trommsdorff (1995), Serpentine stability to mantle depths and subduction-related magmatism, *Science*, *268*, 858–861, doi:10.1126/science.268.5212.858.

van Keken, P. E., B. Kiefer, and S. M. Peacock (2002), High-resolution models of subduction zones: Implications for mineral dehydration reactions and the transport of water into the deep mantle, *Geochem. Geophys. Geosyst.*, *3*(10), 1056, doi:10.1029/2001GC000256.

van Keken, P. E., et al. (2008), A community benchmark for subduction zone modeling, *Phys. Earth Planet. Inter.*, *171*, 187–197, doi:10.1016/j.pepi.2008.04.015.

von Herzen, R., C. Ruppel, P. Molnar, M. Nettles, S. Nagihara, and G. Ekstrom (2001), A constraint on the shear stress at the Pacific-Australian plate boundary from heat flow and seismicity at the Kermadec forearc, *J. Geophys. Res.*, *106*, 6817–6833, doi:10.1029/2000JB900469.

Wada, I. (2009), Thermal structure and geodynamics of subduction zones, Ph.D. thesis, 170 pp., Univ. of Victoria, Victoria, B. C., Canada.

Wada, I., K. Wang, J. He, and R. D. Hyndman (2008), Weakening of the subduction interface and its effects on surface heat flow, slab dehydration, and mantle wedge serpentinization, *J. Geophys. Res.*, *113*, B04402, doi:10.1029/2007JB005190.

Wang, K., and E. E. Davis (1992), Thermal effect of marine sedimentation in hydrothermally active areas, *Geophys. J. Int.*, *110*, 70–78, doi:10.1111/j.1365-246X.1992.tb00714.x.

Wang, K., and J. He (1999), Mechanics of low-stress forearcs: Nankai and Cascadia, *J. Geophys. Res.*, *104*, 15,191–15,205, doi:10.1029/1999JB900103.

Wang, K., and K. Suyehiro (1999), How does plate coupling affect crustal stresses in northeast and southwest Japan?, *Geophys. Res. Lett.*, *26*, 2307–2310, doi:10.1029/1999GL900528.

Wang, K., T. Mulder, G. C. Rogers, and R. D. Hyndman (1995), Case for very low coupling stress on the Cascadia subduction fault, *J. Geophys. Res.*, *100*, 12,907–12,918, doi:10.1029/95JB00516.

Wang, K., I. Wada, and Y. Ishikawa (2004), Stresses in the subducting slab beneath southwest Japan and relation with plate geometry, tectonic forces, slab dehydration, and damaging earthquakes, *J. Geophys. Res.*, *109*, B08304, doi:10.1029/2003JB002888.

White, S. M., J. A. Crisp, and F. J. Spera (2006), Long-term volumetric eruption rates and magma budgets, *Geochem. Geophys. Geosyst.*, *7*, Q03010, doi:10.1029/2005GC001002.

Wilson, D. (1988), Tectonic history of the Juan de Fuca ridge over the last 40 million years, *J. Geophys. Res.*, *93*, 11,863–11,876, doi:10.1029/JB093iB10p11863.

Xia, S., D. Zhao, and X. Qiu (2008), Tomographic evidence for the subducting oceanic crust and forearc mantle serpentinization under Kyushu, Japan, *Tectonophysics*, *449*, 85–96, doi:10.1016/j.tecto.2007.12.007.

Yamasaki, T., and T. Seno (2003), Double seismic zones and dehydration embrittlement of the subducting slab, *J. Geophys. Res.*, *108*(B4), 2212, doi:10.1029/2002JB001918.

Yuan, X., et al. (2000), Subduction and collision processes in the central Andes constrained by converted seismic phases, *Nature*, *408*, 958–961, doi:10.1038/35050073.

Zang, S. X., Q. Y. Chen, J. Y. Ning, Z. K. Shen, and Y. G. Liu (2002), Motion of the Philippine Sea plate consistent with the NUVEL-1A model, *Geophys. J. Int.*, *150*, 809–819, doi:10.1046/j.1365-246X.2002.01744.x.

Zhao, D., A. Hasegawa, and H. Kanamori (1994), Deep structure of Japan subduction zones as derived from local, regional and teleseismic events, *J. Geophys. Res.*, *99*, 22,313–22,329, doi:10.1029/94JB01149.

Zhao, D., T. Matsuzawa, and A. Hasegawa (1997), Morphology of the subducting slab boundary in the northeastern Japan arc, *Phys. Earth Planet. Inter.*, *102*, 89–104, doi:10.1016/S0031-9201(96)03258-X.

Zhao, D., K. Asamori, and H. Iwamori (2000), Seismic structure and magmatism of the young Kyushu subduction zone, *Geophys. Res. Lett.*, *27*, 2057–2060, doi:10.1029/2000GL011512.